Recent sea level changes in the Red Sea: Thermosteric and halosteric contributions, and impacts of natural climate variability

Bayoumy Mohamed [a,b], Nikolaos Skliris [c,*]

[a] *Alexandria University, Faculty of Science, Department of Oceanography, Alexandria, Egypt*
[b] *GeoHydrodynamics and Environment Research (GHER), University of Liège, Liège, Belgium*
[c] *School of Ocean and Earth Science, University of Southampton, Southampton, UK*

ARTICLE INFO

ABSTRACT

This study investigates sea level changes in the Red Sea over the last 29 years (1993–2021) by analyzing long-term trends and interannual variations in the total sea level anomaly (SLA). The study also explores the role of thermosteric and halosteric changes and interannual variability of total SLA using an empirical orthogonal function (EOF) analysis and their relationship with large-scale climate modes. The results show that the trends of total and steric SLA were higher in the northern Red Sea (NRS) than in the southern Red Sea (SRS), influenced by low-salinity water inflow from the Aden Gulf. The average SLA trend in the Red Sea between 1993 and 2021 was about 4.17 ± 0.14 mm/year. However, an abrupt change was observed in SLA and its components, with accelerating trends in the post-2008 period compared to the pre-2008 period. This increase was mainly due to the thermosteric effect, which was positively enhanced throughout the Red Sea. The halosteric component in the NRS contributed negatively to the overall steric effect. The interannual SLA variability accounts for about 45 % of the total variability and can be partially explained by the influence of the El Nino Southern Oscillation.

1. Introduction

Sea level rise due to anthropogenic climate change can have serious consequences for coastal populations and ecosystems around the world. Changes in global mean sea level depend mainly on two factors: the steric effect and mass changes in the water column. The mass changes arise mainly from the interaction between the ocean and the atmosphere, and the inflow of freshwater/ ice melting. Changes in water-column density due to thermal expansion and salinity variations cause worldwide fluctuations in sea level, known as steric sea level (Ishii and Kimoto, 2009; Jordà and Gomis, 2013; Levitus et al., 2012). Steric changes dominate the large-scale sea level variability on seasonal-to-decadal time scales (Gill and Niller, 1973). Quantifying the influence of changes in seawater density on sea level variability is critical for climate change research, as cumulative sea level rise can be considered both a key indicator of climate change and a potential threat to human activities in coastal regions (Storto et al., 2017). Sea level change is neither temporally nor spatially uniform but varies depending on both the time considered and the geographic region (Stammer et al., 2013). To mitigate the impacts of sea level rise on local populations and infrastructure, it is necessary to understand the driving mechanisms and

factors contributing to sea level rise in each specific region. Regional sea level fluctuations can be very dynamic and complex, making it difficult to assess the relative contributions of their driving mechanisms.

The Red Sea is a semi-enclosed marginal sea with great socio-economic importance, being a major shipping route and one of the shortest sea lanes between Europe, the Persian/Arabian Gulf, and East Asia. It has a distinct environmental characteristic in both oceanographic and meteorological aspects. The Red Sea is located between Africa and Asia and is renowned as one of the world's hottest and most saline oceanic regions, owing to its surrounding hot and dry continent, an evaporation rate of ∼ 2 m/year (Nagy et al., 2021; Tragou et al., 1999), negligible river runoff and little precipitation. The southern Red Sea (SRS) is connected to the Aden Gulf and the Indian Ocean through the narrow strait of Bab El-Mandeb (about 25 km wide, with sill-depth of 160 m), whereas the northern Red Sea (NRS) is linked to the Mediterranean Sea via the Suez Canal (see Fig. 1). The study area, which extends from 12.5° N to 30° N and from 32° E to 44° E, has an average depth of 490 m and a maximum centered depth of 1960 m (see, Fig. 1). The Red Sea's coastal areas are characterized by shallow banks, with roughly 40 % of its basin being less than 100 m deep (Rasul et al., 2015).

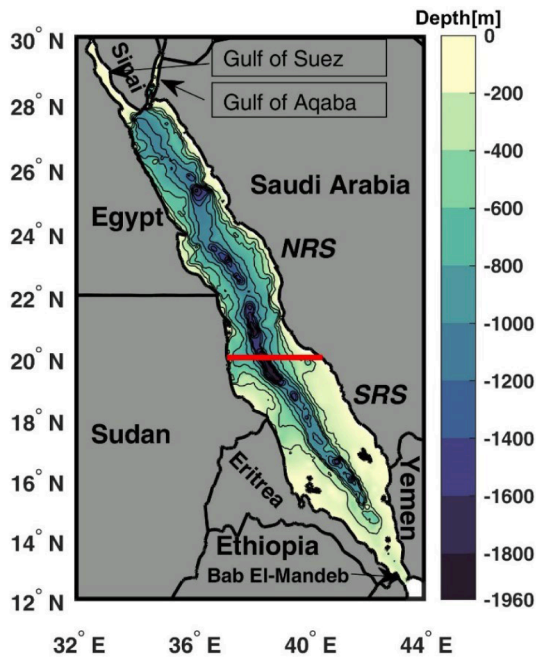Numerous studies have investigated sea level changes on a regional

Fig. 1. Bathymetric map of the Red Sea from the General Bathymetric Chart of the Oceans (GEBCO, https://www.gebco.net/). Based on the wind pattern climatology, the Red Sea was divided into two regions: the northern Red Sea (NRS) and the southern Red Sea (SRS, area south of the solid red line at 20°N). (For interpretation of the references to colour in this figure legend, the reader is referred to the web version of this article.)

scale, including the Red Sea, the Gulf of Aden, and the Arabian Sea, using altimetry and a limited number of tide gauges in these regions. For example, the Aden tide gauge in Yemen is the only tide gauge in the Arabian Peninsula that covers a time window long enough to derive a trend and acceleration in relative sea level (i.e. to account for both land and sea movements). This tide gauge indicated a sea level rise of 3.02 mm/year, based on monthly average sea level data between 1879 and 2011 (Parker and Ollier, 2017). (Al-Subhi and Abdulla (2021) provide a comprehensive analysis of the long-term trend of sea levels in the Red Sea, Arabian Sea, and Arabian/Persian Gulf. They found that the average sea level trends in these three regions between 1993 and 2020 were 3.88 mm/year, 3.16 mm/year, and 2.92 mm/year, respectively. Furthermore, Peter et al. (2022) investigated the variability of surface circulation and chlorophyll distribution in the Arabian Sea and emphasized the impact of Indian Ocean Dipole events on sea level and surface currents.

In recent decades, several studies have focused on seasonal and short-term variations of sea level in the Red Sea (Abdulla and Al-Subhi, 2020; Antony et al., 2022; Churchill et al., 2018; Kusche et al., 2016; Sofianos and Johns, 2001; Sultan et al., 1995; Taqi et al., 2019). These studies concluded that the local surface wind stress and the combined effect of evaporation and water exchange with the Gulf of Aden are the main factors controlling seasonal sea level variations in the Red Sea. However, only a few research papers have evaluated the interannual fluctuations of sea level along the Red Sea coast (Abdulla and Al-Subhi, 2021; Manasrah et al., 2009; Sultan et al., 1996), based on a limited number of tide gauge stations, and could not explain the causes responsible for these variations. Over the last decades, satellite altimetry data have contributed to a better understanding of long-term interannual sea level variations in the Red Sea (Abdulla and Al-Subhi, 2021; Taqi et al., 2020), although altimetry also has limitations, such as land contamination. In recent decades, the quality and accuracy of altimeter data have improved and can be used to study sea level changes along the Red Sea coasts (Taqi et al., 2020, 2019, 2017). They also found that the SLA altimeter data correlate highly with the short-term observations

from three tide gauges along the coast of Sudia Arbia.

The interannual and decadal variability of sea level can be modulated by the large-scale climate variability modes. The two dominant modes of this natural climate variability in the Indo-Pacific region are the El Niño-Southern Oscillation (ENSO) and the Indian Ocean Dipole (IOD) (Li and Han, 2015; Schott et al., 2009). ENSO is the most energetic climate phenomenon on Earth, associated with variations in sea surface temperature (SST) and winds in the tropical Pacific region. IOD is a coupled ocean–atmosphere phenomenon in the equatorial Indian Ocean defined by the difference in SST between the eastern and western parts of the Indian Ocean (Saji et al., 1999; Thompson et al., 2016). Previous studies implied that the heat content and sea level in the Indian Ocean and adjacent regions, such as the Red Sea, are strongly associated with ENSO and IOD (Akhter et al., 2021; Alawad et al., 2019, 2017; Kersalé et al., 2022; Volkov et al., 2020). Recently, it was also found that the Red Sea SST is highly correlated with the Atlantic Multidecadal Oscillation (AMO) index (Krokos et al., 2019). So far, the steric effect in the Red Sea has only been studied on a seasonal scale. For example, (Feng et al., 2014) used coarse resolution temperature/salinity profiles (1°×1°, global grids at monthly intervals) and the Gravity Recovery and Climate Experiment (GRACE) satellite data between 2003 and 2011 to investigate the seasonal variations of the steric effect and the mass-induced sea level. They found that the seasonal variability of sea level is mainly dominated by the mass component.

To fill these gaps, this study focuses on the long-term interannual variability and trends of sea levels in the Red Sea based on satellite altimetry data. Our overarching objective is to understand the causes and factors controlling interannual sea level variability and trends, and to assess the impacts of steric components and associated large-scale coupled atmospheric/oceanic climate modes on sea level change. In particular, we use 29 years (1993–2021) of satellite-derived sea level anomalies (SLA), sea surface temperature and salinity (SST and SSS) data, and 3D reanalysis temperature/salinity profiles over the Red Sea to investigate: (1) the long-term spatiotemporal trends of total SLA, steric effect and its components (thermosteric and halosteric), as well as surface and subsurface temperature and salinity; (2) the relative contributions of thermosteric, halosteric, and total steric effect to interannual SLA variability and trends; (3) the interannual variability of total SLA and the effects of large-scale climate modes of natural variability (i.e., ENSO, IOD, and AMO) on sea level change.

2. Data and methodology

The relative contributions of steric components (thermosteric, and halosteric) and atmospheric effects to interannual sea level variations and trends in the Red Sea were examined using various data sources, as indicated in the following subsections.

2.1. Satellite altimetry and climate indices data

Daily maps of Sea Level Anomalies (SLA) distributed by the Copernicus Marine and Environment Monitoring Service (CMEMS; Doi: 10.48670/moi-00148, accessed June 2023) were used. This dataset is objectively interpolated with a spatial resolution of (0.25°×0.25°) and covers the period from 1993 to 2021. This product is generated by combining multi-satellite altimetry missions (Jason-3, Sentinel-3A, HY-2A, Saral/AltiKa, Cryosat-2, Jason-2, Jason-1, T/P, ENVISAT, GFO, ERS1/2). The data have been subjected to all standard geophysical and environmental adjustments, including instrument errors and tidal influences, as well as dynamic atmospheric correction (DAC), which includes wind and the standard inverted barometer (IB) (Landerer and Volkov, 2013). Here we used the DAC V4.0 only to estimate the contribution of atmospheric forcing on sea level variability, since the satellite altimetry was already atmospherically corrected using the same dataset from AVISO (https://tds.aviso.altimetry.fr/thredds/catalog/dataset-auxiliary-dynamic-atmospheric-correction/catalog.html,

accessed August 2023).

For the glacial isostatic adjustment (GIA) correction, which describes the slow part of the Earth's response to redistribution of mass after the last deglaciation and changes in the shape of ocean basins, we used the rate of change of geoid height (dGeoid) from the ICE $-6G\_C$ (VM5a) model (Peltier et al., 2015) to correct the altimetry data. Both GIA and DAC data are available with a spatial resolution of $(0.25° \times 0.25°)$.

We also used a monthly time series of climate indices representing ENSO, IOD, and AMO climate modes. In this paper, we used the ENSO-Niño3.4 index, defined by the spatial average of the SST anomaly in the Niño3.4 region (120-170°W, 5°N-5°S). Positive $(> +0.5 °C)$ and negative $(< -0.5 °C)$ values of the Niño 3.4 SST index indicate El Niño and La Niña conditions, respectively. IOD is represented by the Dipole Mode Index (DMI), which measures the SST anomaly difference between the western (10°S–10°N, 50°E–70°E) and the eastern (10°S–0°S, 90°E–110°E) parts of the tropical Indian Ocean (Saji et al., 1999). A positive IOD is associated with a large-scale increase (decrease) in surface temperature and precipitation over the western (eastern) part of the tropical Indian Ocean. The AMO is a natural long-term climate variability mode defined by the SST anomaly pattern of the North Atlantic Ocean with a periodicity of 60–80 years (Kerr, 2000). The AMO index used here is a linear detrended, unsmoothed index based on the Kaplan SST dataset (Kaplan et al., 1998). Climate mode data were obtained from the NOAA Physical Sciences Laboratory website (https://psl.noaa.gov/gcos_wgsp/Timeseries/, accessed July 2023).

2.2. SST and SSS datasets

SST and SSS datasets were obtained from the Copernicus Marine Environment Monitoring Service (CMEMS, Doi: 10.48670/moi-00168, accessed January 2023). SST data were derived from the Operational SST and Sea Ice Analyses (OSTIA) dataset (Good et al., 2020) providing daily high-resolution $(0.05° \times 0.05°)$ optimum interpolation data. OSTIA data for the Red Sea were extracted from the global data, providing a 16570-point regularly gridded dataset spanning 10,592 days from January 1993 to December 2021. Monthly sea surface salinity (SSS) fields are derived from the surface global products (https://doi.org/10.48670/moi-00051, last accessed May 2023) distributed by CMEMS. This product is obtained through a multivariate optimal interpolation algorithm that combines Soil Moisture Ocean Salinity (SMOS) satellite images and in situ salinity measurements (Droghei et al., 2018, 2016). This dataset is available at a spatial resolution of $(0.25° \times 0.25°)$ covering the same period (1993–2021). Unless otherwise stated, all data sets used in this study have been converted to monthly averages to ensure consistency.

2.3. ARMOR3D data

The steric effect and its components (thermosteric and halosteric) were calculated using CMEMS high-resolution ARMOR-3D data (https://doi.org/10.48670/moi-00052, last accessed July 2023). The ARMOR-3D dataset contains global 3D quality-controlled monthly profiles of ocean temperature and salinity with a horizontal spatial resolution of $(0.25° \times 0.25°)$ and at standard 50 vertical levels (Guinehut et al., 2012), over the period from 1993 to 2021. This product was obtained through optimal interpolation combining in-situ and satellite observations (Guinehut et al., 2012; Mulet et al., 2012). The in-situ vertical temperature and salinity profiles were obtained by CTD profilers, ARGO buoys, and XBT bathythermographs. Satellite observations include satellite altimetry, sea surface temperature, and salinity. The ARMOR dataset is one of the most reliable products for assessing steric sea level variations (Storto et al., 2017).

2.4. Estimation of steric, thermosteric, and halosteric SLA

Steric SLA (SSLA) was estimated as the vertical integral of the density

anomaly using the ARMOR3D dataset. Subsequently, the steric effect was decomposed into the thermosteric SLA (TSSLA) and the halosteric SLA (HSSLA) using the following formulas, which have also been used in previous studies (Mohamed and Skliris, 2022; Wang et al., 2017), and described in more detail by (Jayne et al., 2003):

$$SSLA = TSSLA + HSSLA = \frac{-1}{\rho_0} \int_{-H}^{0} \Delta\rho \, dz = - \int_{-H}^{0} (\alpha\Delta T - \beta\Delta S) dz$$

Where ρ_0 stands for the reference density (1025 kg/m^3), z for the depth. $\Delta\rho = (\rho_z- \rho)$, $\Delta T = (T_z-T)$, and $\Delta S = (S_z-S)$, where ρ, T, and S are the climatic mean (1993–2021) of density, temperature, and salinity as a function of (longitude, latitude, and depth). ρ_z, T_z, and S_z are the density, temperature, and salinity as a function of depth (i.e. at each layer). α and β are the thermal expansion and saline contraction coefficients, respectively, calculated from monthly temperature and salinity using the Thermodynamic Equation Of Seawater -2010 (TEOS-10) (Pawlowicz et al., 2012), and the Gibbs Sea Water (GSW) Oceanographic Toolbox (McDougall and Barker, 2011). Since the steric effect is mainly due to changes in water density over thermocline depth, the reference depth (H) in this study is set to 700 m or the bottom where the sea is shallower.

2.5. Statistical analysis

The long-term linear trends of the de-seasonalized monthly SLA, SST, SSS, water-column averaged temperature and salinity, and steric components were calculated from 1993 to 2021, using the least-squares method (Wilks, 2011). The estimated trends are tested for statistical significance using the standard two-tailed Modified Mann-Kendall (MMK) test at the 95 % confidence interval (Hamed and Ramachandra Rao, 1998). The corresponding uncertainties (given at 2σ level, i.e. with a 95 % confidence interval) of these trends are estimated using a standard statistical method (Emery and Thomson, 1997), as described in (Mohamed et al., 2019). To detect the abrupt change in SLA, the Pettitt homogeneity test (Pettitt, 1979) was used. The Pettitt test is a nonparametric test commonly used with hydrometeorological variables to determine the occurrence and timing of abrupt and significant changes in the mean of a time series (Manasrah et al., 2009).

To evaluate the dominant spatiotemporal patterns of SLA variability in the Red Sea between 1993 and 2021, the Empirical Orthogonal Function (EOF) analysis (Emery and Thomson, 1997) was carried out. The resulting spatial patterns of variability are known as EOFs, and their temporal evolutions are represented by principal components (PCs) time series. Prior to computing the EOFs, the monthly mean SLAs were removed, de-seasonalized using a monthly mean seasonal climatology and a 13-month running mean, and detrended locally (i.e., at each grid point) to focus on the interannual to decadal variation in sea level. The time series were then normalized (i.e., each point time series was divided by its standard deviation) to avoid a point of high variability dominating the analysis (Mohamed et al., 2022). The derived PCs were further correlated with the large-scale climate indices (ENSO, IOD, and AMO) to investigate their co-variability in the Red Sea. The MATLAB program R2020b and Climate Data Toolbox (CDT) (Greene et al., 2019) were used to estimate the long-term trends, remove seasonal cycles, apply the MMK test, and perform the EOF analysis.

3. Results and discussion

3.1. Annual mean climatology and seasonal cycles of SST, SSS, and sea level

The annual climatological mean values of SST, SSS, and sea level over the Red Sea between 1993 and 2021 are shown in Fig. 2. Both SST and SSS show high spatial variability in their climatological mean values, with a clear SSS gradient towards the north (i.e., a meridional
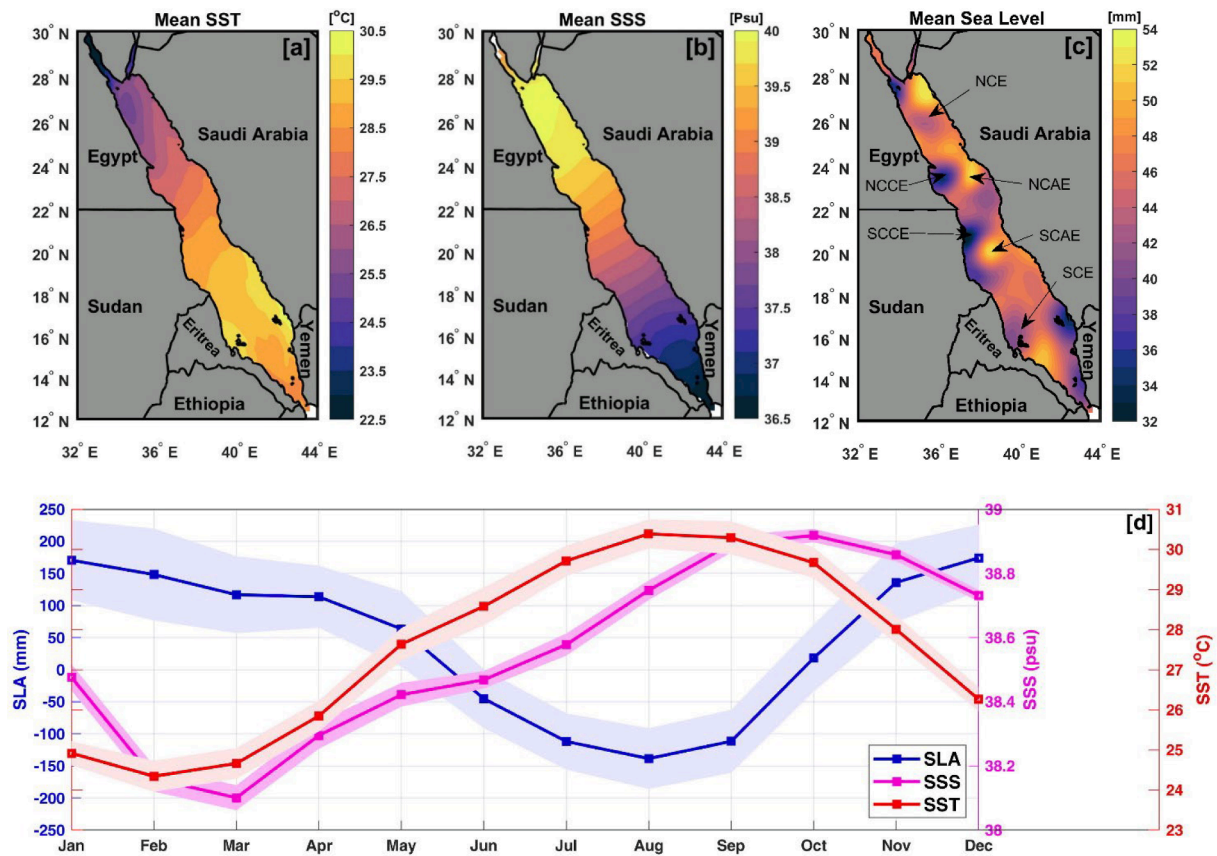
Fig. 2. Climatological annual means (a) sea surface temperature, (b) sea surface salinity, and (c) sea level between 1993 and 2021. (d) Climatological mean seasonal cycle of sea level anomaly (blue line), sea surface temperature (red line), and salinity (magenta line). The shaded areas represent ± standard deviation for each data set. Abbreviations in (c) refer to the north-central and south-central anticyclonic eddy (NCAE and SCAE), the north-central and south-central exhibited cyclonic eddy (NCCE and SCCE), and the north and south cyclonic eddy (NCE and SCE). (For interpretation of the references to colour in this figure legend, the reader is referred to the web version of this article.)

increasing gradient from south to north), where it reaches its maximum value (up to 40 psu) in the northern part of the Red Sea and the lowest value (36.5 psu) in the southern part of the Red Sea (Fig. 2b). The opposite is true for SST, which also exhibits a meridional gradient, but with the lowest values in the north and the highest in the south. The SST pattern is more complicated and shows its maximum in the region between the northern coast of Eritrea and the southern coast of Saudi Arabia and decreases toward the two ends of the Red Sea (Fig. 2a). These results are consistent with (Sofianos and Johns, 2003), who attribute this pattern to the very weak wind speed in the same region, which has a higher SST where the wind field is convergent most of the year.

The annual climatology of sea level shows that sea level is generally higher on the eastern boundary than on the western boundary (Fig. 2c). The observed isolated patches (higher or lower values of SLA) indicate the presence of frequent mesoscale eddies in this region, with maximum values corresponding to regions with anticyclonic eddies, such as the anticyclonic eddies on the eastern side of the north-central and south-central Red Sea (NCAE and SCAE). The lowest values occurred in the regions that exhibited cyclonic eddies, such as the cyclonic eddies on the west side of the north-central and south-central Red Sea (NCCE and SCCE) and in the northern and southern Red Sea (NCE and SCE, see their locations in Fig. 2c). The positions of these eddies are well defined by (Raitsos et al., 2013; Sofianos and Johns, 2007, 2003; Taqi et al., 2019; Zhan et al., 2019).
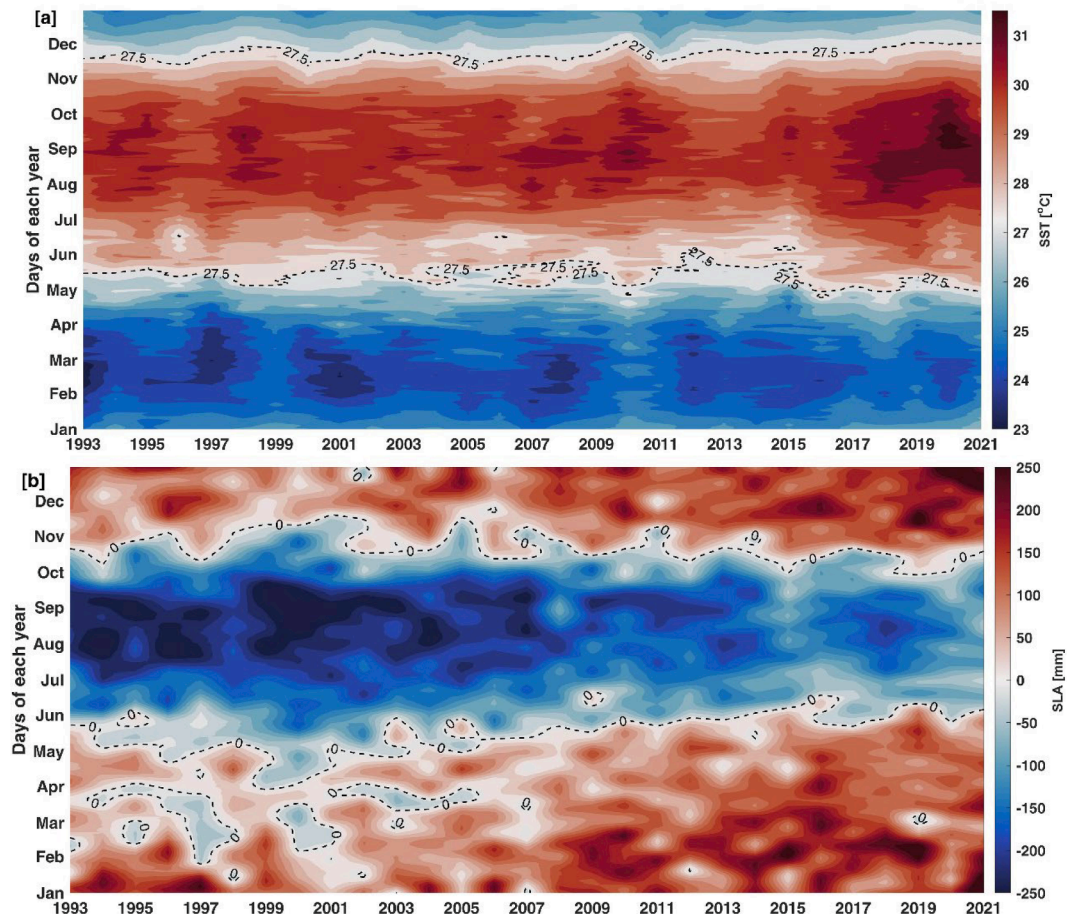
The climatologically mean seasonal cycles of SST, SSS, and SLA (Fig. 2d) show that the general seasonal cycle of SSS follows that of SST, with a one-month lag for SSS. The highest SST was observed from July to October, while the highest SSS was observed from August to November.

The lowest SST was observed from January to April, while the lowest SSS was found from February to May. The seasonal cycle of SLA in the Red Sea shows an opposite variation to SST: the highest values of SLA are observed in winter (December to February), while the lowest values are observed in summer (July to September). These results are consistent with previous studies (Antony et al., 2022; Sofianos and Johns, 2001; Sultan et al., 1995). The seasonal cycle of SLA followed a similar pattern from south to north of the Red Sea (Fig. S1). The amplitudes of seasonal variability of SST, SSS, and SLA are 6.3 °C, 0.7 psu, and 30 cm, respectively. Previous studies have shown that the wind is the most important factor controlling the seasonal variability of SLA (Sofianos and Johns, 2007), followed by evaporation (Nagy et al., 2021; Sultan et al., 1995).

Regional mean SST and SLA time series were formed by averaging daily data from all grid points in the Red Sea throughout the analyzed period from 1993 to 2021 and plotted using a Hovmöller diagram to investigate changes in the seasonal cycle of the two variables (Fig. 3). Overall, the SST and SLA were dominated by significant increases between 1993 and 2021, especially during warm seasons (see Fig. 3). Increasing sea surface warming during the warm/summer season caused a phenological shift in the seasonal cycle with a significant increase toward a warmer and longer summer season (Fig. 3a and Fig. S2), resulting in a shortening of the period during which SLA was negative during the warm season (Fig. 3b). Note that SLA is always negative during the warm/summer season (i.e., SST and SLA are anticorrelated), indicating that the seasonal variability of SLA in the Red Sea is driven by factors other than SST.

The comparison of the seasonal SLA cycles in the Red Sea with those

Fig. 3. Hovmöller diagram of spatially averaged (over the entire Red Sea) daily (a) SST and (b) SLA annual variations, indicating changes in seasonal cycles between 1993 and 2021. The black contour lines show the climatological mean values of SST (27.5 °C) and SLA (0 mm). (For interpretation of the references to colour in this figure legend, the reader is referred to the web version of this article.)

of the Arabian Sea and the Persian Gulf shows that the pattern of seasonal sea level variability in the Red Sea differs significantly from that of these two basins. The possible reason for this is the different influence of the wind on the sea level (Al-Subhi and Abdulla, 2021). In the Red Sea, the wind blows from the NNW in summer, which increases the outflow of water from the Red Sea and thus lowers the sea level. In winter, the wind in the SRS turns SSE and increases the inflow of water into the Red Sea, causing the sea level to rise. The wind in the NRS is relatively weak in winter (Antony et al., 2022). The difference in wind patterns and influences is therefore the main reason for the observed difference in the seasonal SLA cycle between the Red Sea and the Arabian Sea (Al-Subhi and Abdulla, 2021). Based on the wind pattern climatology(Antony et al., 2022), the observed gradient of mean SST and SSS (Fig. 2a and b), and the interannual variability of SLA, we divided the Red Sea into two regions (NRS and SRS), using 20°N as the general boundary between these two regions (Fig. 1). This division is useful to study the temporal variability and trend in NRS and SRS separately and in contrast to each other.

3.2. Surface and subsurface temperature and salinity changes

Linear trend maps of SST and SSS and the water column-averaged (0–700 m depth) temperature and salinity are shown in Fig. 4. Statistically significant (p < 0.05) positive SST trends are observed over the entire Red Sea between 1993 and 2021 (Fig. 4a). However, this trend is not uniform across the region and exhibits high spatial variability, ranging from 0.005 to 0.035 °C/year. The highest SST trend is found in the deep region in the middle of the Red Sea (Fig. 4a), while the lowest

SST trend is found in the southernmost part of the Red Sea (i.e., between Yemen and the southern coast of Eritrea) and along the coastal regions, in addition to the regions with recurrent cyclonic eddies, such as the NCE, SCE, NCCE, and SCCE. The spatial pattern of the SST trend is similar to that reported by (Mohamed et al., 2021) although they used a longer period (1982–2019). A lower, but still significant, trend in water-column averaged (0–700 m depth) temperatures is observed over the entire Red Sea (Fig. 4c), following the accelerating SST warming. The influence of cyclonic and anticyclonic eddies on the observed temperature trend below the surface is more pronounced than at the sea surface, with the trend being lower for cyclonic eddies and higher for anticyclonic eddies (Fig. 4c).

SSS was found to be decreasing throughout most of the Red Sea, especially along the eastern boundary, with the strongest negative SSS trends at the two ends of the Red Sea and in regions with anticyclonic eddies (e.g., NCAE and SCAE) (Fig. 4b). The positive SSS trends are only observed along the western boundary (along the southern Egyptian, Sudanese, and northern Eritrean coasts), especially in the cyclonic eddies (e.g., NCCE, SCCE, and SCE), which could be due to the upwelling of high salinity water to the surface, contributing to an increase in surface water salinity in these regions. In contrast, water column-averaged salinity shows a positive (but mostly statistically non-significant) trend in most parts of the region. The exception is the two ends of the Red Sea, where a significant negative salinity trend is obtained (Fig. 4d). The contrasting trends in surface and subsurface salinity could be due to higher evaporation rates increasing salt deposition and thus salinity in the subsurface, while the negative trend in surface salinity could be due to the influx of less saline water from the
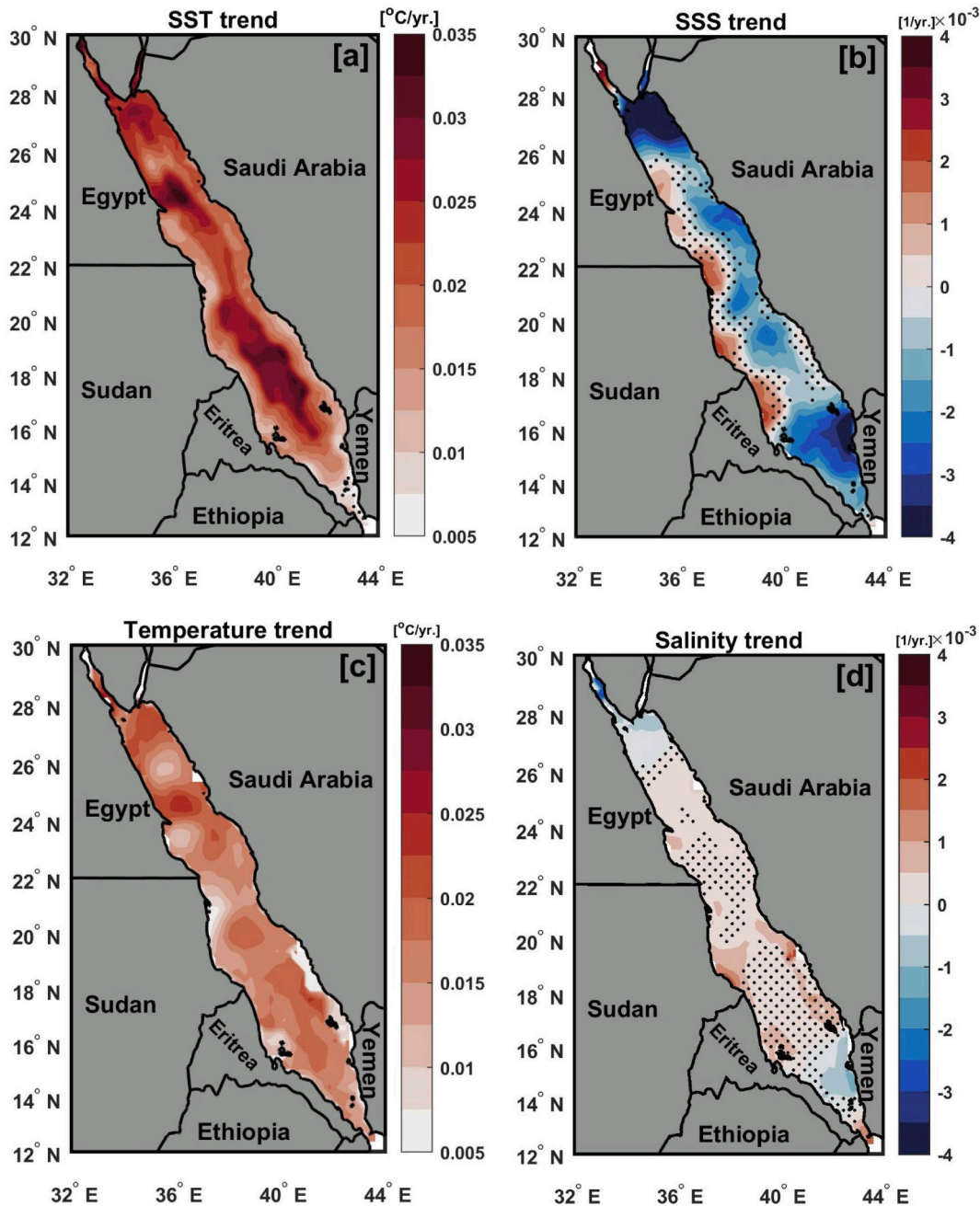
Fig. 4. Spatial trend maps over the Red Sea between 1993 and 2021 for (a) SST, (b) SSS, and (c, d) averaged water column (from 0 to 700 m) temperature and salinity. Regions where trends are statistically non-significant at the 95 % confidence interval are shown in black dots. (For interpretation of the references to colour in this figure legend, the reader is referred to the web version of this article.)

Gulf of Aden into the surface layer; in addition, surface wind and precipitation could play a role in some regions. However, further analysis and data are needed to investigate the role of general circulation and winds in the variability of surface salinity and sea level changes in the Red Sea.

The de-seasoned (i.e., the mean seasonal cycle removed) time series of spatially averaged (SST, SSS, and averaged water column temperature and salinity) over the Red Sea and its sub-basins between 1993 and 2021 are shown in Fig. 5. The temporal trend of SST and SSS show that there is no significant difference between their trend values in the NRS and SRS, with an average trend of 0.02 ± 0.003 °C/year and −0.001 ± 0.000 psu/year, respectively, for SST and SSS in the entire Red Sea between 1993 and 2021. The SST trend is consistent with (Mohamed et al., 2021) for the period 1982–2019. Compared to the trend for the entire period,

the SST trend after 2008 is approximately double for NRS, quadruple for SRS, and triple for the entire Red Sea (Fig. 5 and Table 1). This amplified warming trend after 2008 was largely influenced by the rapid increase in SST over the last decade (black lines in Fig. 5). The spatial mean values of water column temperature and salinity show positive statistically significant trends of 0.01 ± 0.001 °C/year and 0.001 ± 0.000 psu/year, respectively. Although interannual variability plays an important role, the trend for both parameters appears to be accelerating in the last decade (2012–2021) as a result of increasing atmospheric warming and evaporation rates (Nagy et al., 2021).

3.3. Sea level trends from satellite altimetry and its components

In this section, we analyze in detail the spatiotemporal evolution and
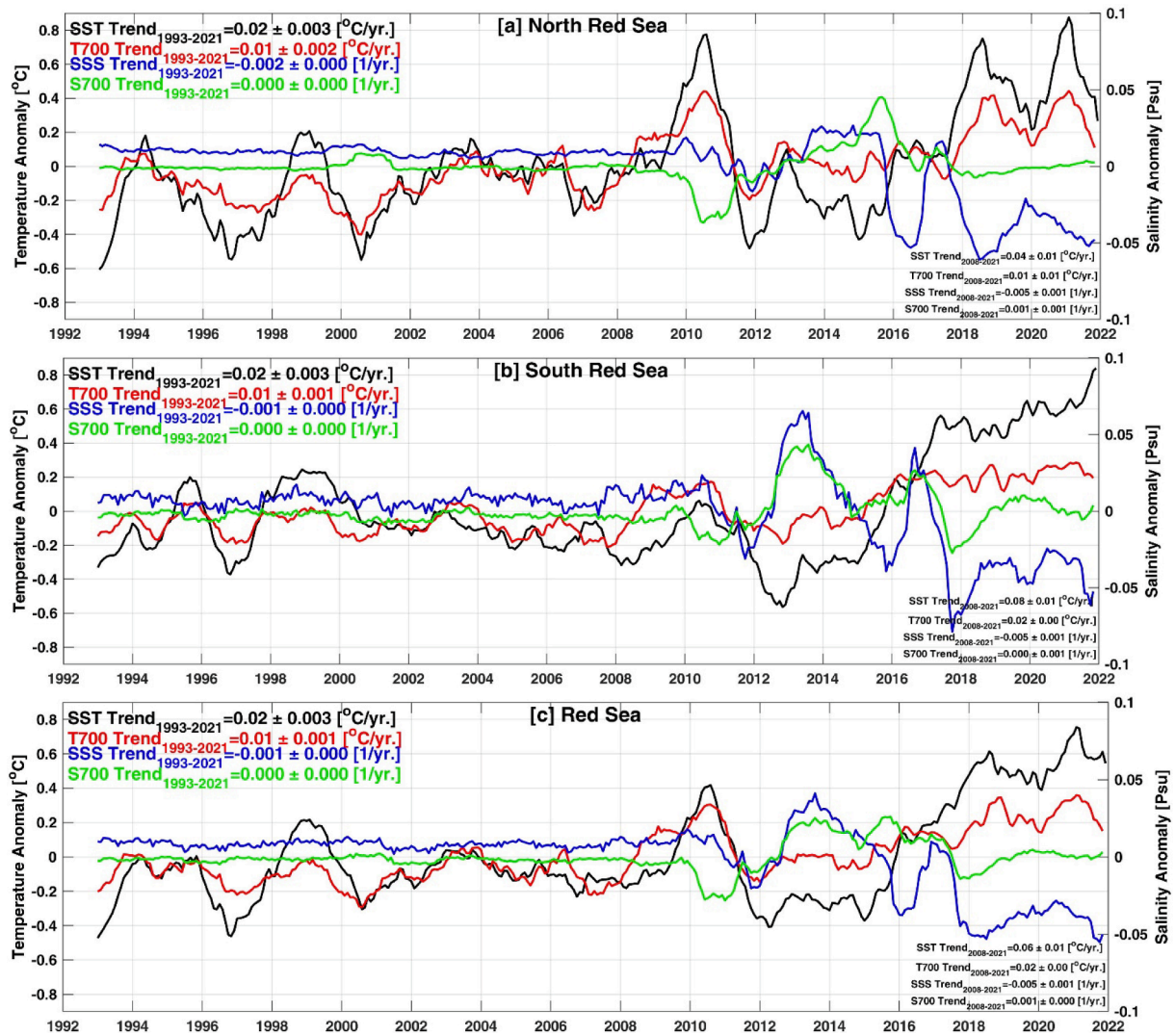
Fig. 5. Temporal variations and linear trends of de-seasoned monthly fields of sea surface temperature (SST, black lines), spatially averaged 3-D temperature above 700 m (T700, red lines), sea surface salinity (SSS, blue lines), and spatially averaged 3-D salinity above 700 m (S700, green lines) between 1993 and 2021; for the (a) northern and (b) southern regions of the Red Sea and (c) the entire Red Sea. The trend values for each variable over the entire period and after 2008 are also shown. All-time series are low-pass filtered with a 13-month cutoff period. (For interpretation of the references to colour in this figure legend, the reader is referred to the web version of this article.)

Table 1
Summary of the long-term trend of SST (°C/year) and sea level anomaly (SLA) and its components (mm/year) for the northern and southern Red Sea (NRS and SRS) and the entire Red Sea (RS) throughout the full period (1993–2021) and the post-2008 period. The non-significant trends are highlighted by underlining (p values > 0.05).

	Full Period			Post-2008		
	NRS	SRS	RS	NRS	SRS	RS
SST	0.02 ± 0.003	0.02 ± 0.003	0.02 ± 0.003	0.04 ± 0.01	0.08 ± 0.01	0.06 ± 0.01
SLA	4.24 ± 0.16	4.10 ± 0.13	4.17 ± 0.14	4.20 ± 0.29	4.78 ± 0.28	4.48 ± 0.27
Steric SLA (SSLA)	2.01 ± 0.14	1.19 ± 0.06	1.61 ± 0.10	0.90 ± 0.41	1.40 ± 0.21	1.14 ± 0.29
Residual SLA (RSLA)	2.05 ± 0.11	2.69 ± 0.09	2.36 ± 0.10	3.12 ± 0.39	3.14 ± 0.26	3.13 ± 0.32
Thermosteric SLA (TSSLA)	2.15 ± 0.14	1.18 ± 0.06	1.68 ± 0.10	1.44 ± 0.40	1.57 ± 0.19	1.50 ± 0.28
Halosteric SLA (HSSLA)	– 0.14 ± 0.02	_0.00 ± 0.01_	– 0.07 ± 0.01	– 0.54 ± 0.07	– 0.17 ± 0.05	–0.36 ± 0.06

long-term trend of the total SLA from altimetry, thermosteric, and halosteric effect from the reanalysis dataset over the period from 1993 to 2021. Then we estimate the relative contributions of the total steric effect and its components (thermosteric and halosteric) to the overall sea level variability. The altimetry SLA trend map of the Red Sea between 1993 and 2021 is shown in Fig. 6a. A statistically significant (p < 0.05) SLA trend is observed throughout the Red Sea. However, this trend is not uniform across the region and exhibits high spatial variability, ranging from 1.5 to 5.5 mm/year. The strongest SLA trend is observed in the NRS and in regions with anticyclonic eddies (e.g., NCAE and SCAE). The lowest SLA trends are found in the regions with cyclonic eddies (e.g., NCE, NCCE, SCCE, and SCE). The trend of the total SLA spatially averaged over the entire Red Sea is 4.21 ± 0.59 mm/year. This trend is higher than the observed rate of global mean sea level rise of 3.33 ± 0.33 mm/year, for the same period (Cazenave and Moreira, 2022). This trend is also slightly higher than the SLA trend of 3.88 mm/year observed by (Abdulla and Al-Subhi, 2021) in the Red Sea for the period 1993–2020, and by (Mohamed and Skliris, 2022) in the adjacent eastern Mediterranean (3.1 ± 0.61 mm/year) for the period 1993–2019. The atmospheric contribution to the observed sea level trend due to atmospheric pressure and wind components (i.e., DAC) from 1993 to 2021 in
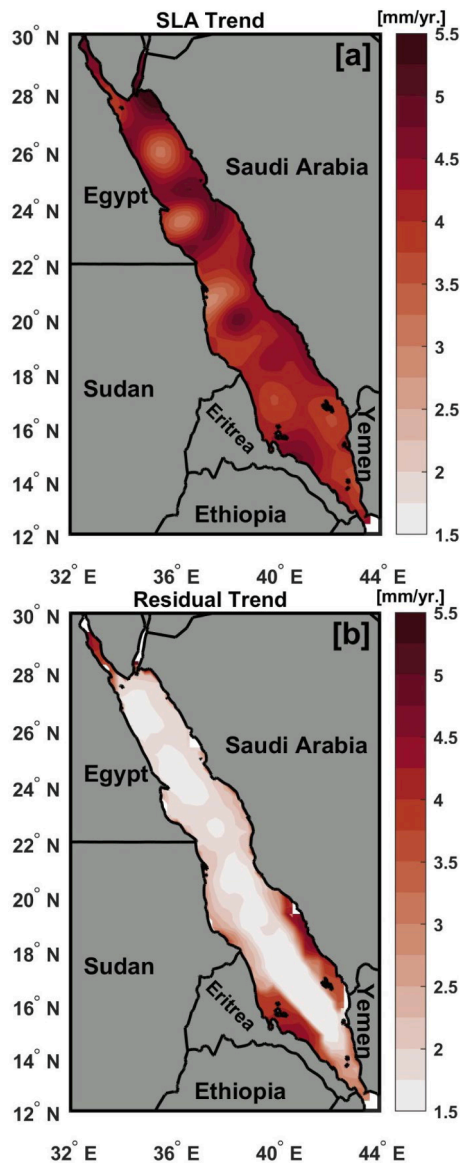
Fig. 6. Map of sea level anomaly trends (mm/year) for the period between 1993 and 2021 from (a) altimetry, (b) altimetry after removal of total steric effect and GIA correction (residual). Mean and seasonal cycles were removed from the time series at each grid point. Note that the estimated trends are statistically significant (95% confidence interval) for the entire region for both SLA and the residual.

the Red Sea is negligible, as the trends in atmospheric contribution are not significant on both temporal and spatial scales throughout the Red Sea (Fig. S3).

The residual SLA trend map is shown in Fig. 6b. These trends are estimated after subtracting the total steric effect and the GIA correction. The GIA correction to the altimetry data (dGeoid) is negative and very small over the entire Red Sea, ranging from −0.09 to −0.13 mm/year (Fig. S4), with an average of −0.11 mm/year. The residual SLA trend includes the contribution of oceanic mass change and redistribution, changes in bottom pressure that can be caused by ocean currents (Dangendorf et al., 2021; Landerer et al., 2007), and local vertical land movements, such as sediment loading or compaction. Groundwater extraction and tectonics may also contribute to the residual trend. The highest values of the residual SLA trend are found in the shallow regions (<100 m) in the southeast and southwest parts of the southern Red Sea (Fig. 6b), which are mainly influenced by the inflow of water from the

Gulf of Aden through the Bab El-Mandeb strait and in the Gulf of Suez influenced by the Suez Canal. The rest of the Red Sea shows a smaller but still significant increase in the residual of the SLA trends (Fig. 6b), indicating that the main cause of the observed long-term sea level trends is the steric effect. The average spatial trend of the residuals of SLA for the entire Red Sea is 2.36 ± 0.62 mm/year. These results indicate that the inferred mass component is the strongest contributor to sea level development in the southern Red Sea, while the steric component has the strongest effect in the NRS.

The spatial trend maps of the total steric sea level effect and its components (i.e., the thermosteric and halosteric sea level) are shown in Fig. 7. Statistically significant positive trends in the total steric and thermosteric sea level are observed throughout the Red Sea (Fig. 7a and b). These patterns are consistent with the observed trend from the total SLA (Fig. 6a) and can largely be explained by temperature variations (i. e., the thermosteric effect), except for the shallow water regions in the southeast and southwest parts of the SRS and the Gulf of Suez, which show a small steric effect, as the steric effect is a depth integral. The spatial average of the steric sea level trend over the whole Red Sea is 1.6 ± 0.50 mm/year, which explains about 38 % of the total sea level trend (4.21 mm/year). The thermosteric effect has an average trend of 1.65 ± 0.57 mm/year and explains most of the steric trend, accounting for about 40 % of the total sea level trend.

The halosteric effect in the Red Sea varied between negative significant trends (up to −0.5 mm/year) in the NRS and positive significant trends (up to + 0.3 mm/year) in the southeastern Red Sea (mainly along the Yemen region), while non-significant trends were found between these two regions (Fig. 7c). The positive halosteric trend in the southern region could be due to mixing with less saline water from the Gulf of Aden (Sofianos and Johns, 2003). Compared to the estimated trend values of the steric components, the spatial pattern of their trend uncertainty (Fig. S5) shows that the trend uncertainty of the total steric and thermosteric component is less than 0.5 mm/year, while it was less than 0.1 mm/year for the halosteric component over most of the Red Sea.

The temporal variability of the mean SLA and its components in the NRS, SRS, and total Red Sea between 1993 and 2021 is analyzed here (Figs. 8, 9, 10, and Table 1). From the de-seasoned monthly SLA time series and based on Pettitt's homogeneity test (Fig. 8), it is evident that there has been a significant abrupt change in the entire Red Sea since 2008. Sea level over the entire Red Sea and its sub-basins (NRS and SRS) have changed from a period of episodic negative anomalies and a non-significant trend (1993–2007; see Table S1) to positive anomalies and a significantly higher trend in the post-2008 period (Fig. 8a-c). This abrupt change could be due to sea level recovery from the strong negative sea level anomaly associated with successive strong/weak La Nina events in 2007/2008 and 2008/2009. The monthly cumulative SLA time series over the entire Red Sea and its sub-basins show a prevalence of negative anomalies in the pre-2008 period and a prevalence of positive anomalies in the post-2008 period (Fig. 8d). Looking at monthly cumulative sea level anomalies (Fig. 8d), 2008 was the year with the strongest and most negative anomalies during the study period. These changing trends are indicative of the shift observed in 2008. These changing trends are an indication of the shift observed in 2008. However, this shift was observed in 2004 over the North Indian Ocean (Srinivasu et al., 2017), which could be due to the limitation of the study period (1993–2013).

Fig. 9 shows the temporal evaluation of the overall mean SLA, the steric sea level of the upper layer, and the residual time series in the NRS, SRS, and the overall Red Sea. All-time series are low-pass filtered with a 13-month cutoff period for better comparability and to highlight interannual variability. Strong interannual and decadal variations in regionally averaged SLA are observed in the Red Sea and its sub-basins between 1993 and 2021. The filtered SLA shows a decreasing sea level until 2000, in agreement with (Abdulla and Al-Subhi, 2021). However, according to the Pettitt test, this year is not recognized as an abrupt turning point. Several increases and decreases in sea level were observed
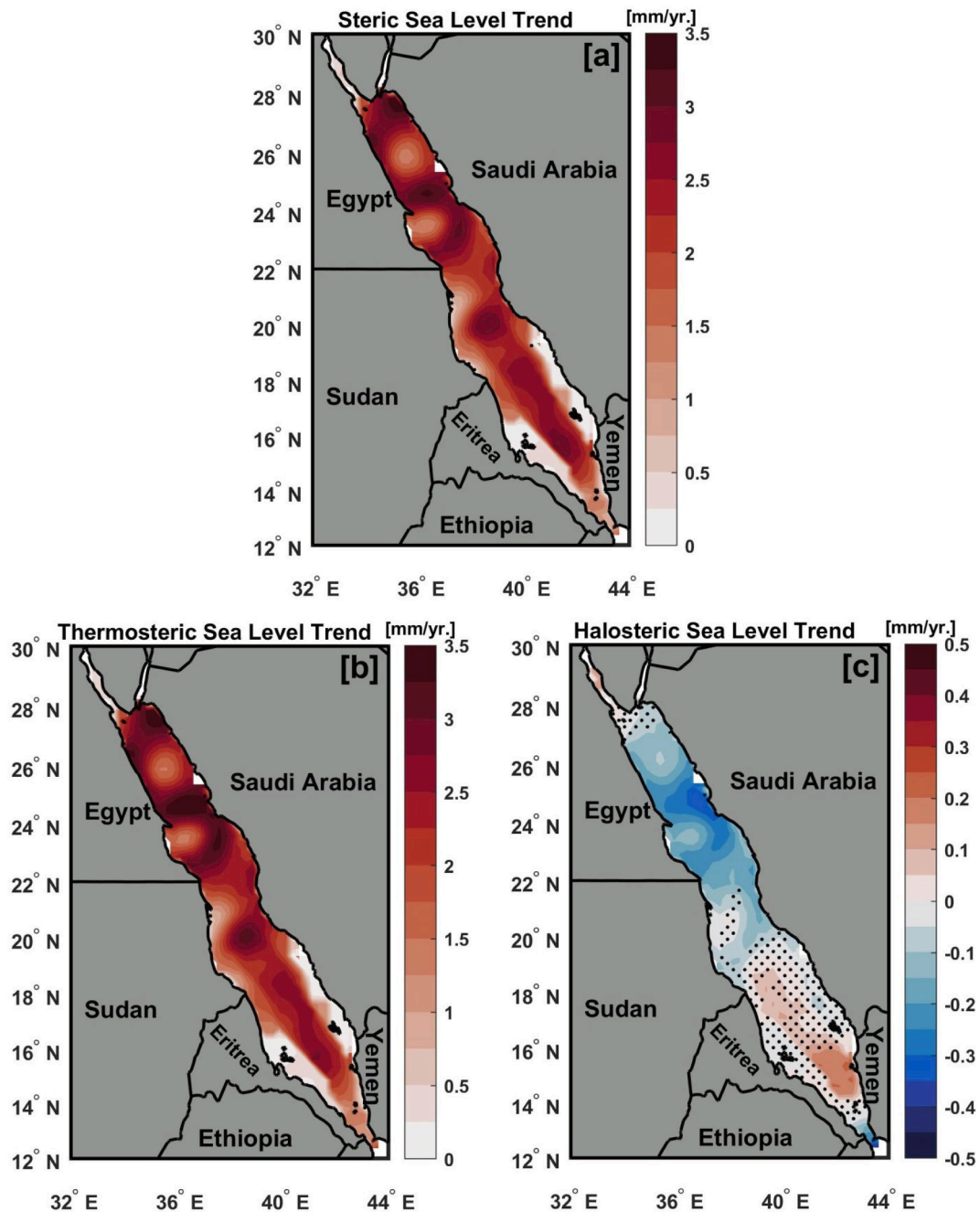
Fig. 7. Spatial patterns of trends (mm/year) of (a) total steric, (b) thermosteric, and (c) halosteric components from above 700 m depth during 1993–2021. Mean and seasonal cycles were removed from all-time series at each grid point. Black stippling indicates areas where the trends are statistically non-significant at the 95 % confidence interval.

in the interannual signal, with the highest SLA rises in 2016 and 2021, while the largest falls were observed in 2000 and 2007. Trend analysis also shows an abrupt increase in the total sea level, steric sea level, and residuals in the post-2008 period. Linear trends of SLA for the different periods (total period, pre-2008, and post-2008) were estimated separately and superimposed in Fig. 8. The significance test showed that the increasing trends in the post-2008 period were statistically significant, while the pre-2008 trends were non-significant (p > 0.05; see Table S1).

The similarity in SLA patterns between the NRS and SRS after 2008 confirms the possible role of the observed climate shift and the amplified warming on the sea level changes across the entire region, while the differences in SLA patterns before 2008 could be due to different regional influences or local phenomena that affected SLA patterns

differently in the two regions. It is clear from Table S1 that the steric component in the NRS showed a very small but still significant negative trend, while the residual component contributed positively to the SLA trend in the SRS. The opposite contribution of these two components could be the reason for the different SLA variability between NRS and SRS before 2008.

The overall trend in total SLA for the NRS and SRS is 4.24 ± 0.16 mm/year and 4.10 ± 0.13 mm/year, respectively. However, the trend observed in the SRS was much higher in the post-2008 period, with a value of 4.78 ± 0.28 mm/year (Fig. 9b and Table 1). In comparison, it did not change for the NRS (4.20 ± 0.29 mm/year, see Fig. 9a). The average trend of total SLA for the entire Red Sea is 4.17 ± 0.14 mm/year for the entire period (1993–2021) and 4.48 ± 0.27 mm/year for the
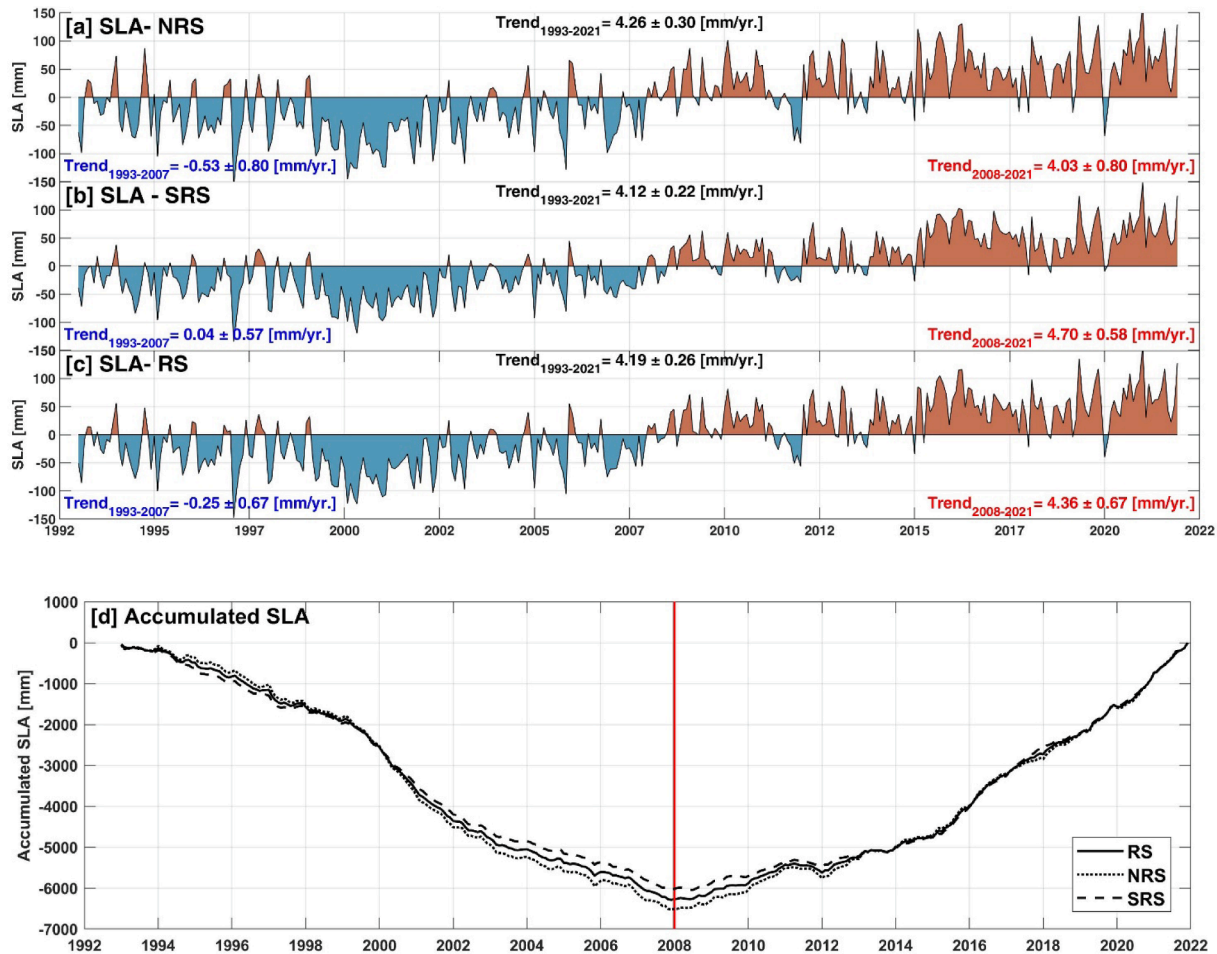
Fig. 8. Time evolution of regionally averaged de-seasoned monthly mean sea level anomalies over (a) the northern Red Sea (NRS), (b) the southern Red Sea (SRS), and (a) the entire Red Sea (RS) between 1993 and 2021. (d) Long-term variation of cumulative sea level anomalies in the same areas (see Fig. 1). The vertical red line represents the corresponding year (2008) of abrupt sea level change. The linear trend value (mm/year) for each region for the different time periods is also indicated. (For interpretation of the references to colour in this figure legend, the reader is referred to the web version of this article.)

post-2008 period (Fig. 9c). In the NRS, both the steric and inferred mass (i.e., residual) components contribute equally (with a value of about 2 mm/year) to the overall SLA trend throughout the entire study period (Fig. 9a), while in the SRS the mass contribution is higher than the steric effect (Fig. 9b). This could be due to the inflow of water through the Bab El-Mandeb strait. In general, the inferred mass component shows greater variability and a stronger trend than the steric component throughout the entire Red Sea (Fig. 9c and Table 1).

The partitioning of the total steric effect into the thermosteric and halosteric effects in the NRS and SRS (Fig. 10a-b) shows that the enhanced sea level rise is mainly due to the thermosteric effect, which has greater variability and a much stronger trend, especially in the NRS (Fig. 10a). The thermosteric trend is 2.15 ± 0.14 mm/year and 1.18 ± 0.06 mm/year for the NRS and SRS, respectively, with an average trend of 1.68 ± 0.10 mm/year for the entire Red Sea (Fig. 10c). The halosteric component shows a significant negative contribution only in the second period (i.e., after 2008), while in the period before 2008 both the thermosteric and halosteric components show negative and a non-significant trend (see Table S1). In the post-2008 period, the halosteric trend is -0.54 ± 0.07 mm/year and -0.17 ± 0.05 mm/year for the NRS and SRS, respectively, with an average trend of -0.36 ± 0.06 mm/year for the entire Red Sea (Fig. 10a-c and Table 1). This also indicates that the highest halosteric trend was in the NRS, which can be attributed to the increased salinity of the water column in this region (Fig. 4d).

3.4. Sea level interannual variability and relationship to large-scale climate modes

To estimate the interannual variability of sea level, we estimated the average percentage of the ratio between the root mean square (RMS) of the interannual signal (i.e., the de-seasoned and detrended signal) and the total (seasonal and non-seasonal) sea level. The total sea level variability (i.e., root mean square, RMS) over the entire Red Sea between 1993 and 2021, ranges from 9.5 to 15.5 cm, with a basin mean of 13 cm (see Fig. 11a). The greatest variability in total sea level is observed along the eastern boundary (particularly along the coasts of Saudi Arabia and northern Yemen). The sea level interannual variability (i.e., the de-seasoned and detrended signal) exhibits a RMS range of variation between 4.5 and 7.5 cm, with a spatial mean of 5.9 cm (see Fig. 11b). The highest interannual sea level variability is found in the two anticyclonic eddies in the northern and southern center of the Red Sea, while the lowest interannual sea level variability is found at the southern entrance of the Red Sea and in the cyclonic eddies in the northern and southern Red Sea (Fig. 11b). On average, interannual sea level variability accounts for 45 % of the total sea level variability in the Red Sea, with a range of 35 to 60 % (Fig. 11c).

The power spectrum of the de-seasoned and detrended sea level time series throughout the Red Sea is calculated using Welch's method (Welch, 1967) and is shown in Fig. S6. The spectra are plotted on a logarithmic scale to highlight a wider range of sea level variability (Mohamed et al., 2022). After removing the seasonal variability by the
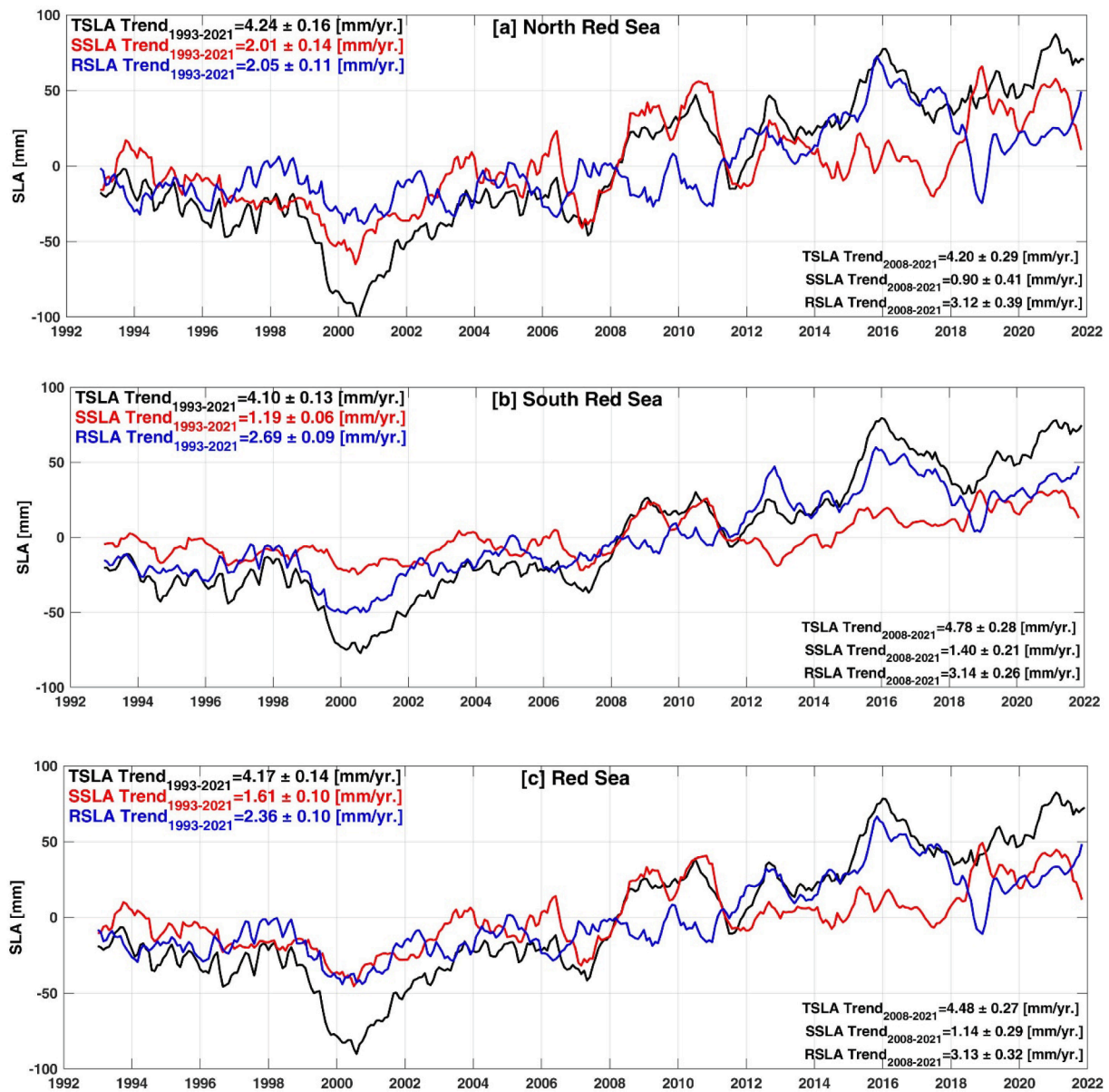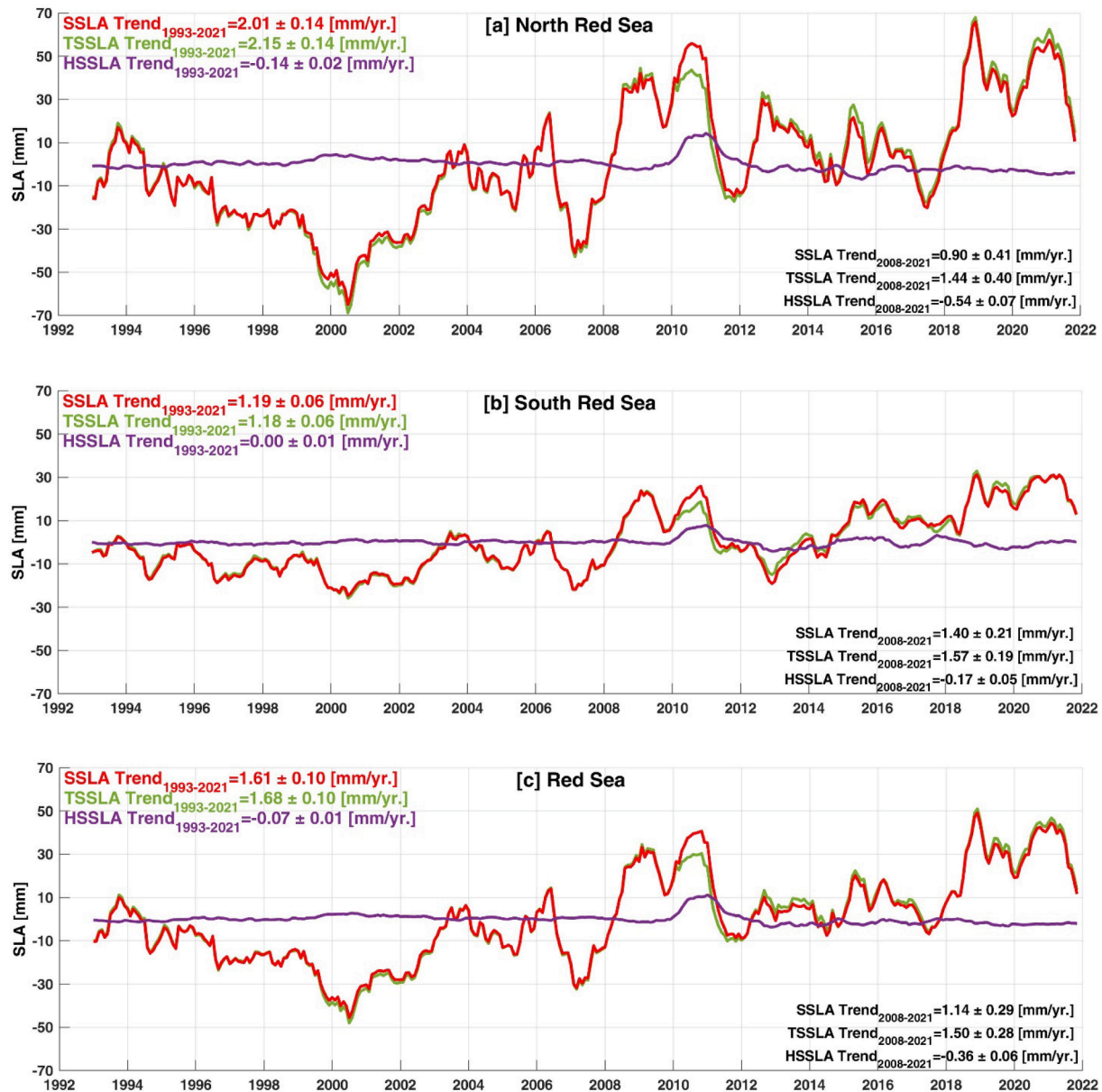
Fig. 9. Temporal variations of the total mean sea level anomaly (TSLA, black lines), the steric sea level anomaly (SSLA, red lines), and the residual component (difference between the total SLA and the steric effect) of the sea level anomaly (RSLA, blue lines) between 1993 and 2021; for the (a) northern and (b) southern regions of the Red Sea and (c) the entire Red Sea. The trend values (mm/year) for each variable over the entire period and after 2008 are also shown. All-time series are low-pass filtered with a 13-month cutoff period. (For interpretation of the references to colour in this figure legend, the reader is referred to the web version of this article.)

13-month running mean, the variability can be divided into three frequency ranges: the interannual cycle, the decadal cycle, and the multi-decadal cycle. This spectrum shows two basic peaks on the interannual time scale, the first peak is found with a periodicity between 3–4 years (centered at 3.6 years), and the second peak between 5–7 years (centered at 6.1 years). These two cycles could be related to ENSO, which can cause oscillations between 3 and 7 years (Manasrah et al., 2009). Another periodicity of about 22 years is observed in the Red Sea (Fig. S6), which is related to the double sunspot cycle (11 years) (Kane and Trivedi, 1985). This result is consistent with (Manasrah et al., 2009), who found the same peak in the simulated sea level at the Port Sudan station in the Red Sea.

The spatially coherent SLA interannual variability is estimated using EOF analysis. The first two EOF modes of SLA account for about 82 % of the total interannual variability. The spatial distribution of the first SLA EOF (EOF1) leading mode (which accounts for about 76.6 %) has a

positive value over the entire Red Sea (Fig. 12a), indicating an in-phase sea level rise over the entire Red Sea. The highest SLA spatial variability is found over most of the southern Red Sea, while the lowest variability is found over the deep region in the middle and at the southern entrance of the Red Sea. The spatial distribution of the second SLA EOF (EOF2) mode, which explains about 5.4 % of the total de-seasoned variance (Fig. 12b), shows a meridional dipolar (i.e., out-of-phase) oscillation with a nodal line around 20°N and opposite variations between the NRS and SRS (i.e., positive anomalies over the NRS and negative anomalies over the SRS). The greatest variability is found in the NRS, while the opposite maximum variability is found in the SRS. This dipolar structure is consistent with that observed for the Red Sea SST, with 20°N serving as the boundary between the two regions (Karnauskas and Jones, 2018; Mohamed et al., 2021).

The temporal coefficients of PC1 and PC2, corresponding to the EOF modes and reflecting variation over the study period, are shown as black

Fig. 10. Temporal variations of the total steric sea level anomaly (SSLA, red lines) and contributions of the thermosteric sea level anomaly (TSSLA, green lines) and halosteric sea level anomaly (HSSLA, purple lines) between 1993 and 2021; for the (a) northern and (b) southern regions of the Red Sea and (c) the entire Red Sea. The trend values (mm/year) for each variable over the entire period and after 2008 are also shown. All-time series are low-pass filtered with a 13-month cutoff period. (For interpretation of the references to colour in this figure legend, the reader is referred to the web version of this article.)

and green lines in Fig. 12c. PC1 captures the interannual and decadal variability of SLA with a pronounced alternation of positive and negative peaks on an interannual time scale with a period of 3–7 years (black line in Fig. 12c). The highest variability is observed in 1993 and 2016, and the lowest in 2000 and 2007, which coincide with the positive (i.e., El Niño events) and negative (i.e., La Niña events) phases of ENSO, respectively. The PC2 time series exhibits lower variability with smooth variations, in particular, during the first period (i.e., until 2008, see green line in Fig. 12 c), consistent with the very low percentage of explained SLA variance. The highest peak of PC2 in 2010 coincides with a strong positive phase of IOD, while the lowest negative peak in 2017 is associated with a weak IOD and La Niña events.

To further investigate the relationship between sea level variability and various climate modes (ENSO, IOD, and AMO), we examined the correlation between the PC1 time series of SLA and the normalized climate indices (Fig. 12c). During the whole study period, a statistically

significant positive correlation of 0.52 was found only between PC1 and ENSO with a lag of 7–9 months (i.e., ENSO index occurs first, see Fig. S7), whereas AMO and IOD showed a non-significant correlation (p > 0.05). However, after 1998 (i.e., during the period from 1998 to 2021), when the AMO index reversed from the negative to the positive phase (Mohamed et al., 2023), both AMO and IOD showed significant correlations with PC1 of 0.48 and 0.60, respectively. However, the correlation with the AMO index should be taken with caution as our study period (29 years) is shorter than the typical cycle of the AMO index (60–80 years).

El Niño conditions and the strong positive phases of IOD (Fig. 12c) that occurred in 1997/1998, 2009/2010, 2015/2016, and 2019 are associated with a positive value of PC1 and SLA. The strongest sea level response to ENSO was observed during the strongest El Niño event, which occurred in 2015/2016 and was also associated with a strong positive phase of IOD (see blue line in Fig. 12c). The observed SLA
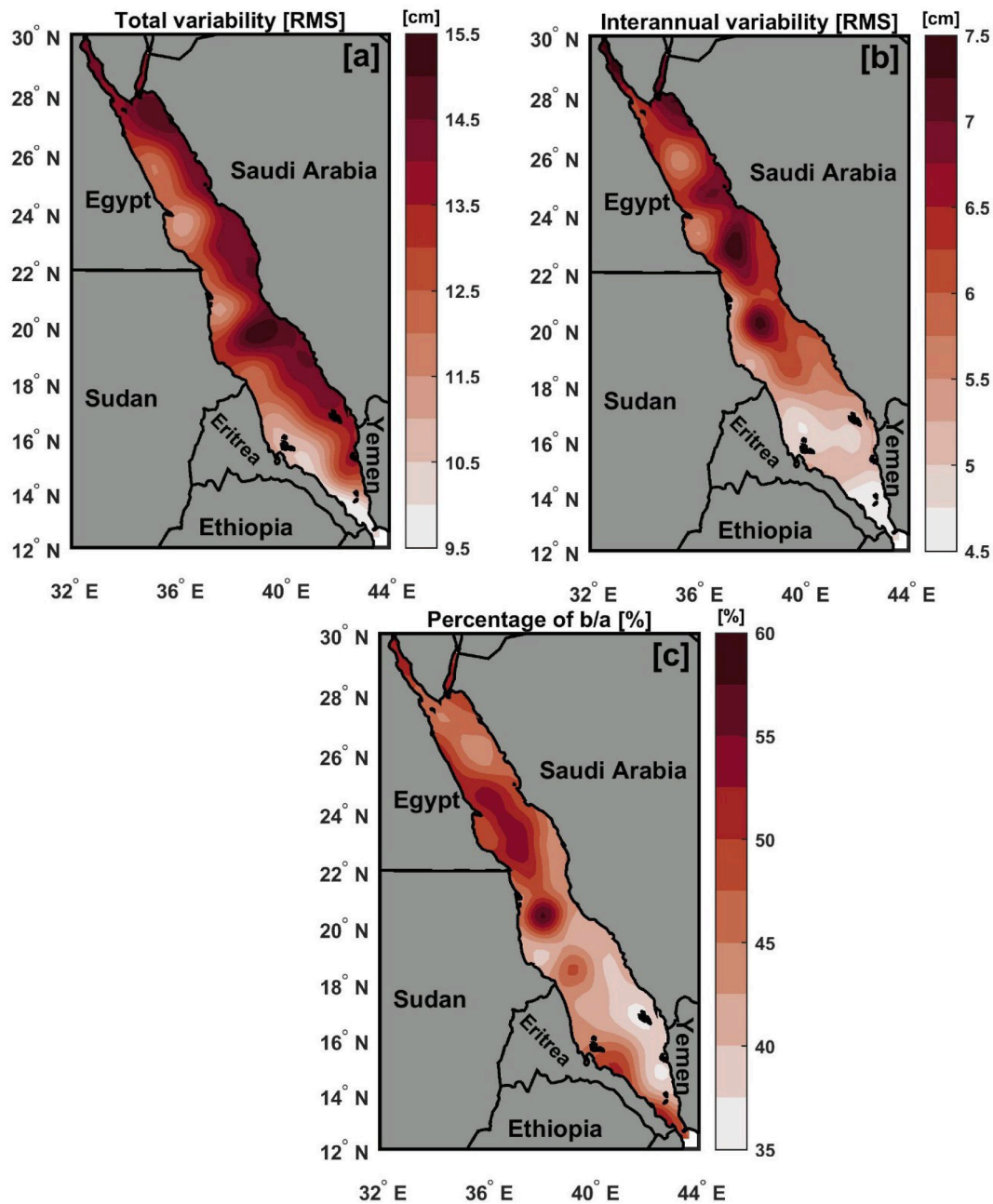
Fig. 11. Total (a) and interannual (b) sea level variability (root mean square, RMS in cm) over the Red Sea between 1993 and 2021. (c) The percentage of the sea level interannual variability (i.e., the percentage of the ratio between [b] and [a]). (For interpretation of the references to colour in this figure legend, the reader is referred to the web version of this article.)

variability was due to an anomalous high-pressure system in the western Pacific Ocean during the El Niño event, which enhanced easterly winds in the equatorial Indian Ocean and led to a positive SLA in the western equatorial Indian Ocean and surrounding regions, including the Red Sea (Abdulla and Al-Subhi, 2021; Saji et al., 2006). During La-Niña events and negative or weaker IOD years (e.g., 1999/2001, 2007/2008, 2011/2012, and 2017/2018), a significant decrease in SLA was observed in the Red Sea. This could be due to the intensification of the low-pressure system in the western Pacific during La-Niña, leading to an intensification of westerly winds in the equatorial Indian Ocean. This generally induces a negative SLA in the western equatorial Indian Ocean and the southwestern Arabian Sea (Abdulla and Al-Subhi, 2021; Saji et al., 2006), which in turn may result in a negative SLA in the Red Sea. The strong La-Niña event in 2011 was associated with a sharp drop in global mean sea level and regional changes in precipitation patterns (Boening

et al., 2012). The significant correlation found here between the AMO index and SLA in the Red Sea after 1998, when the thermosteric effect appears to be a major driver of SLA variability, is consistent with (Krokos et al., 2019), who found a robust correlation between AMO and SST in this region.

4. Summary and conclusions

In this study, our overarching goal was to understand the causes and factors controlling the observed sea level changes in the Red Sea over the last three decades, and to assess the impact of steric components and associated large-scale coupled atmospheric/oceanic climate modes on sea level change. Specifically, we examined the long-term spatiotemporal trend patterns and interannual variability of observed altimetric sea levels, the thermohaline structure of the upper ocean, and the role of
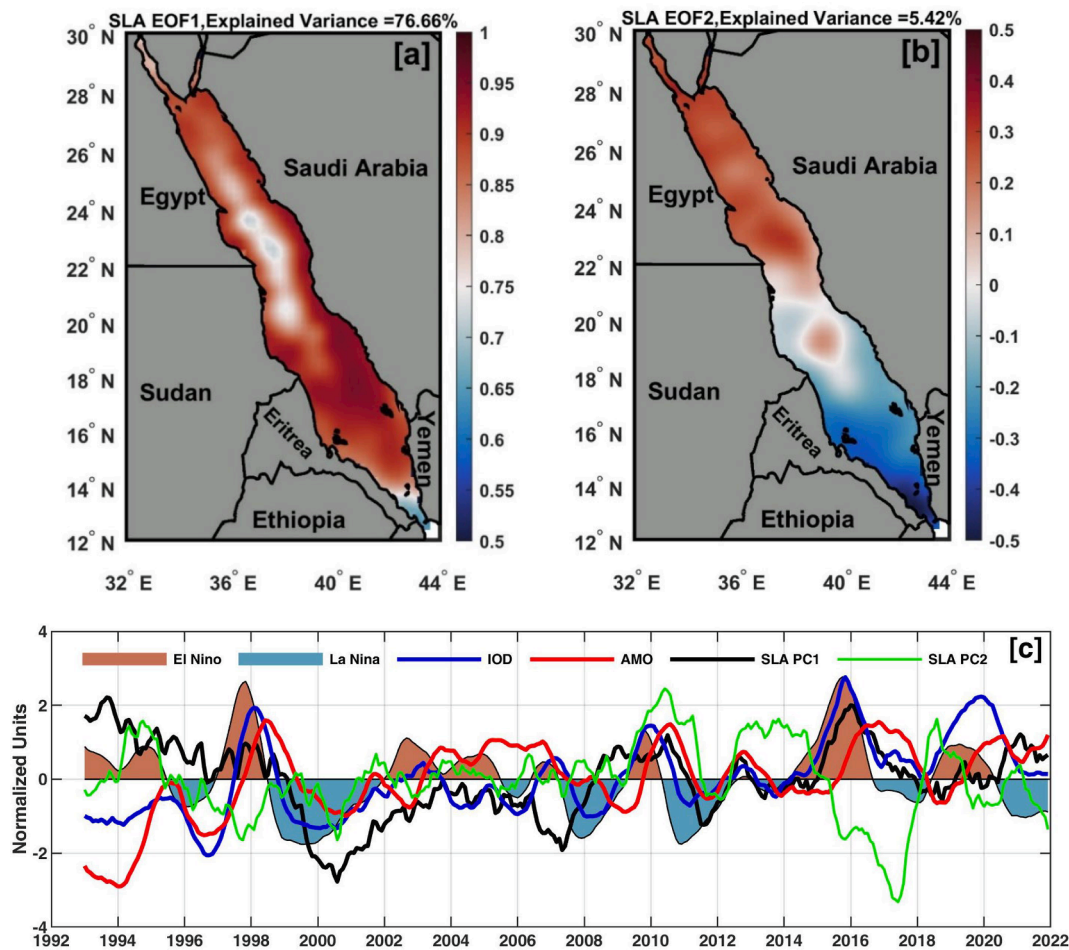
Fig. 12. (a, b) Spatial distribution of the first two EOF modes. (c) The corresponding time series of the principal components (PC1 and PC2, black and green lines, respectively) of the SLA interannual variability (trend and seasonal cycles have been removed) in the Red Sea over the period from 1993 to 2021. The time series of the monthly normalized ENSO Niño3.4 index (El Niño and La Niña are represented by red and blue shading, respectively), the IOD index (blue line), and the AMO index (red line) are also shown. All-time series were low pass filtered with a 13-month period after removing the seasonal climatology and then normalized. (For interpretation of the references to colour in this figure legend, the reader is referred to the web version of this article.)

thermosteric and halosteric changes. Then, the observed interannual variability of sea level was related to large-scale climate modes (i.e., ENSO, IOD, and AMO). The main results and conclusions are summarized below.

Analysis of the climatology and seasonal cycle of sea level, SST, and SSS showed that the highest climatological mean values over 1993–2021 for the SST were in the SRS and the lowest values were in the NRS, while the opposite was true for the SSS due to the inflow of low-salinity water from the Gulf of Aden into the SRS. The climatological mean values of SLA captured the main cyclonic and anticyclonic eddies in the Red Sea (Fig. 2). The seasonal cycle of SLA and SST in the Red Sea showed opposite variations, with the lowest/highest values of SLA /SST in summer (July to September) and the highest/lowest values of SLA/ SST in winter (December to February). The seasonal cycle of SSS follows that of SST, with a one-month lag for SSS. The amplitudes of seasonal variability of SST, SSS, and SLA were about 6.3 °C, 0.7 psu, and 30 cm, respectively. Our results of seasonal variation support findings that were well documented in several previous studies (Abdulla and Al-Subhi, 2021; Antony et al., 2022; Sofianos and Johns, 2003)). Therefore, we focused here mainly on the interannual and long-term variability, that was not fully elucidated in these previous studies, especially regarding the thermosteric and halosteric contributions to SLA change.

The analysis of long-term trends showed that the spatial patterns of the linear trends of total SLA, SST, steric and thermosteric SLA were statistically significant over each grid point in the Red Sea (Fig. 4a, 6a, 7

a-b), while the halosteric effect showed significant negative trends in the NRS and non-significant trends in the SRS (Fig. 7c and Table 1). The highest trends of the total SLA, steric, and thermostatic effect were found in the anticyclonic eddy regions and the lowest in the cyclonic eddy regions (Fig. 6a, 7a-b). The temporal trend of SLA and SST showed that there was no significant difference between their trend values in the NRS and SRS, with an average trend of 4.17 ± 0.14 mm/year and 0.02 ± 0.003 °C/year for SLA and SST, respectively, over the entire Red Sea between 1993 and 2021. An abrupt change in SLA and its components was observed throughout the Red Sea, with accelerated trends in the post-2008 period compared to the pre-2008 period, which showed non-significant trends (see Table S1). These amplified trends could be due to sea level recovery from the strong negative sea level anomaly associated with successive strong/weak La Nina events in 2007/2008 and 2008/ 2009 (Fig. 8, Fig. 12c). The contribution of the steric effect to the observed overall trend of SLA was about 50 % in the NRS and 30 % in the SRS. The increase in the trend of SLA was mainly due to the thermostatic effect, which was positively enhanced throughout the Red Sea with an average trend of 2.15 ± 0.14 and 1.18 ± 0.06 mm/year for the NRS and SRS, respectively. In contrast, the halosteric component in the NRS contributed negatively to the overall steric SLA with a small but still significant negative trend of –0.14 ± 0.02 mm/year and a non-significant trend in the SRS. These results are consistent with previous studies in the North Indian Ocean (Palanisamy et al., 2014; Parekh et al., 2017; Salim et al., 2012), which have shown that the thermosteric effect

was the main cause of sea level variability and trend in this region.

The interannual variability of SLA accounts for about 45 % of the total variance (Fig. 11b), with higher interannual variability in the two anticyclonic eddies in the northern and southern center of the Red Sea, while the lowest interannual variability of sea level was found at the southern entrance and in the cyclonic eddies in the northern and southern parts of the basin (Fig. 11b). Apart from the SLA interannual variability, a multi-year (about 3–7 years) oscillation in the SLA is observed associated with ENSO and IOD events.

EOF analysis was conducted to evaluate the interannual and long-term variability of sea level in the Red Sea between 1993 and 2021 (Fig. 12). The results showed that the first EOF explains about 77 % of the total non-seasonal variance. The spatial distribution pattern of this mode captures an in-phase fluctuation of SLA over the entire Red Sea (i. e., positive SLA). The second EOF mode (which explains about 5 % of the total non-seasonal variance) indicates a dipole structure with out-of-phase variability between NRS and SRS. On the interannual time scale, significant correlations were found between the first principal component (PC1) and the Nino3.4 index with a lag of 7–9 months (i.e., the ENSO index occurs first). The IOD and AMO were significantly correlated with PC1 only after 1998, after the reversal of the AMO index from negative to positive phase. In general, the SLA in the Red Sea showed a significant variation with different phases of these climate mode indices. The positive SLA coincides with the warm ENSO phase (El Niño events) and positive IOD, while the negative SLA occurred during the cold ENSO phase (La Niña events) and negative IOD events. The same is true for the AMO index, but its effect is more pronounced on a multidecadal time scale. Our results indicate that the Red Sea SLA variability throughout the 29-year study period can be partially attributed to atmospheric changes driven by the ENSO, IOD, and AMO climate modes.

Overall, the results of this study provided a better understanding of the factors contributing to regional sea level variations and trends in the Red Sea, including thermosteric and halosteric effects, and the large-scale natural climate variability modes. Our research outcomes can be used to improve model prediction of the sea state from regional short-term weather/ocean forecasting applications to long-term climate projections. Further research using ongoing observations and ocean and coupled climate models is needed to investigate the broader implications of sea level rise and quantify all the components of the sea level budget in this region. This is particularly important for the coastal environment and near-shore areas where vital socioeconomic activities occur.

CRediT authorship contribution statement

Bayoumy Mohamed: Writing – review & editing, Writing – original draft, Visualization, Validation, Supervision, Software, Resources, Project administration, Methodology, Investigation, Funding acquisition, Formal analysis, Data curation, Conceptualization. **Nikolaos Skliris:** Writing – review & editing, Visualization, Validation, Supervision, Software, Resources, Project administration, Methodology, Investigation, Funding acquisition, Formal analysis, Data curation, Conceptualization.

Declaration of competing interest

The authors declare that they have no known competing financial interests or personal relationships that could have appeared to influence the work reported in this paper.

Appendix A. Supplementary material

Supplementary data to this article can be found online at https://doi.org/10.1016/j.pocean.2025.103416.

Data availability

Data will be made available on request.

References

Abdulla, C.P., Al-Subhi, A.M., 2020. Sea Level Variability in the Red Sea: A Persistent East–West Pattern. Remote Sensing 2020, Vol. 12, Page 2090 12, 2090. Doi: 10.3390/RS12132090.

Abdulla, C.P., Al-Subhi, A.M., 2021. Is the Red Sea Sea-Level Rising at a Faster Rate than the Global Average? An Analysis Based on Satellite Altimetry Data. Remote Sensing 2021, Vol. 13, Page 3489 13, 3489. Doi: 10.3390/RS13173489.

Akhter, S., Qiao, F., Wu, K., Yin, X., Chowdhury, K.M.A., Chowdhury, N.U.M.K., 2021. Seasonal and long-term sea-level variations and their forcing factors in the northern Bay of Bengal: a statistical analysis of temperature, salinity, wind stress curl, and regional climate index data. Dyn. Atmos. Oceans 95, 101239. https://doi.org/10.1016/J.DYNATMOCE.2021.101239.

Alawad, K.A.I., Al-Subhi, A.M., Alsaafani, M.A., Alraddadi, T.M., 2017. Signatures of tropical climate modes on the Red Sea and Gulf of Aden sea level. Indian J. Geo-Mar. Sci. 46.

Alawad, K.A., Al-Subhi, A.M., Alsaafani, M.A., Alraddadi, T.M., Ionita, M., Lohmann, G., 2019. Large-Scale Mode Impacts on the Sea Level over the Red Sea and Gulf of Aden. Remote Sensing 2019, Vol. 11, Page 2224 11, 2224. Doi: 10.3390/RS11192224.

Al-Subhi, A.M., Abdulla, C.P., 2021. Sea-level variability in the arabian gulf in comparison with global oceans. Remote Sens. (Basel) 13. https://doi.org/10.3390/rs13224524.

Antony, C., Langodan, S., Dasari, H.P., Abualnaja, Y., Hoteit, I., 2022. Sea-level extremes of meteorological origin in the Red Sea. Weather Clim. Extrem. 35, 100409. https://doi.org/10.1016/J.WACE.2022.100409.

Boening, C., Willis, J.K., Landerer, F.W., Nerem, R.S., Fasullo, J., 2012. The 2011 la Nia: so strong, the oceans fell. Geophys. Res. Lett. 39. https://doi.org/10.1029/2012GL053055.

Cazenave, A., Moreira, L., 2022. Contemporary sea-level changes from global to local scales: a review. Proceedings of the Royal Society A 478. Doi: 10.1098/RSPA.2022.0049.

Churchill, J.H., Abualnaja, Y., Limeburner, R., Nellayaputhenpeedika, M., 2018. The dynamics of weather-band sea level variations in the Red Sea. Reg. Stud. Mar. Sci. 24, 336–342. https://doi.org/10.1016/j.rsma.2018.09.006.

Dangendorf, S., Frederikse, T., Chafik, L., Klinck, J.M., Ezer, T., Hamlington, B.D., 2021. Data-driven reconstruction reveals large-scale ocean circulation control on coastal sea level. Nat. Clim. Chang. 11. https://doi.org/10.1038/s41558-021-01046-1.

Droghei, R., Buongiorno Nardelli, B., Santoleri, R., 2016. Combining in situ and satellite observations to retrieve salinity and density at the ocean surface. J. Atmos. Ocean Technol. 33, 1211–1223. https://doi.org/10.1175/JTECH-D-15-0194.1.

Droghei, R., Nardelli, B.B., Santoleri, R., 2018. A new global sea surface salinity and density dataset from multivariate observations (1993-2016). Front. Mar. Sci. 5, 84. https://doi.org/10.3389/FMARS.2018.00084/BIBTEX.

Emery, W.J., Thomson, R.E., 1997. Data analysis methods in physical oceanography. Data Anal. Methods Phys. Oceanogr. https://doi.org/10.1016/S0167-5370.

Feng, W., Lemoine, J.M., Zhong, M., Hsu, H.T., 2014. Mass-induced sea level variations in the Red Sea from GRACE, steric-corrected altimetry, in situ bottom pressure records, and hydrographic observations. J. Geodyn. 78, 1–7. https://doi.org/10.1016/J.JOG.2014.04.008.

Gill, A.E., Niller, P.P., 1973. The theory of the seasonal variability in the ocean. Deep-Sea Res. Oceanogr. Abstr. 20, 141–177. https://doi.org/10.1016/0011-7471(73)90049-1.

Good, S., Fiedler, E., Mao, C., Martin, M.J., Maycock, A., Reid, R., Roberts-Jones, J., Searle, T., Waters, J., While, J., Worsfold, M., 2020. The current configuration of the OSTIA system for operational production of foundation sea surface temperature and ice concentration analyses. Remote Sens. (Basel) 12. https://doi.org/10.3390/rs12040720.

Greene, C.A., Thirumalai, K., Kearney, K.A., Delgado, J.M., Schwanghart, W., Wolfenbarger, N.S., Thyng, K.M., Gwyther, D.E., Gardner, A.S., Blankenship, D.D., 2019. The climate data toolbox for MATLAB. Geochem. Geophys. Geosyst. 20, 3774–3781. https://doi.org/10.1029/2019GC008392.

Guinehut, S., Dhomps, A.L., Larnicol, G., Le Traon, P.Y., 2012. High resolution 3-D temperature and salinity fields derived from in situ and satellite observations. Ocean Sci. 8, 845–857. https://doi.org/10.5194/OS-8-845-2012.

Hamed, K.H., Ramachandra Rao, A., 1998. A modified Mann-Kendall trend test for autocorrelated data. J. Hydrol. (Amst.) 204, 182–196. https://doi.org/10.1016/S0022-1694(97)00125-X.

Ishii, M., Kimoto, M., 2009. Reevaluation of historical ocean heat content variations with time-varying XBT and MBT depth bias corrections. J. Oceanogr. 65, 287–299. https://doi.org/10.1007/s10872-009-0027-7.

Jayne, S.R., Wahr, J.M., Bryan, F.O., 2003. Observing ocean heat content using satellite gravity and altimetry. J. Geophys. Res. Oceans 108, 1–12. https://doi.org/10.1029/2002jc001619.

Jordà, G., Gomis, D., 2013. On the interpretation of the steric and mass components of sea level variability: The case of the Mediterranean basin. J. Geophys. Res. Oceans 118, 953–963. https://doi.org/10.1002/jgrc.20060.

Kane, R.P., Trivedi, N.B., 1985. Periodicities in sunspot numbers. J. Geomag. Geoelec. 37, 1071–1085. https://doi.org/10.5636/JGG.37.1071.

Kaplan, A., Cane, M.A., Kushnir, Y., Clement, A.C., Blumenthal, M.B., Rajagopalan, B., 1998. Analyses of global sea surface temperature 1856–1991. J. Geophys. Res. Oceans 103, 18567–18589. https://doi.org/10.1029/97JC01736.

Karnauskas, K.B., Jones, B.H., 2018. The interannual variability of sea surface temperature in the Red Sea from 35 years of satellite and in situ observations. J. Geophys. Res. Oceans 123, 5824–5841. https://doi.org/10.1029/2017JC013320.

Kerr, R.A., 2000. A North Atlantic climate pacemaker for the centuries. Science 1979 (288), 1984–1986. https://doi.org/10.1126/SCIENCE.288.5473.1984.

Kersalé, M., Volkov, D.L., Pujiana, K., Zhang, H., 2022. Interannual variability of sea level in the southern Indian Ocean: Local vs. remote forcing mechanisms. Ocean Sci. 18, 193–212. https://doi.org/10.5194/OS-18-193-2022.

Krokos, G., Papadopoulos, V.P., Sofianos, S.S., Ombao, H., Dybczak, P., Hoteit, I., 2019. Natural climate oscillations may counteract Red Sea warming over the coming decades. Geophys. Res. Lett. 46, 3454–3461. https://doi.org/10.1029/2018GL081397.

Kusche, J., Uebbing, B., Rietbroek, R., Shum, C.K., Khan, Z.H., 2016. Sea level budget in the Bay of Bengal (2002–2014) from GRACE and altimetry. J. Geophys. Res. Oceans 121, 1194–1217. https://doi.org/10.1002/2015JC011471.

Landerer, F.W., Jungclaus, J.H., Marotzke, J., 2007. Ocean bottom pressure changes lead to a decreasing length-of-day in a warming climate. Geophys. Res. Lett. 34. https://doi.org/10.1029/2006GL029106.

Landerer, F.W., Volkov, D.L., 2013. The anatomy of recent large sea level fluctuations in the Mediterranean Sea. Geophys. Res. Lett. 40, 553–557. https://doi.org/10.1002/grl.50140.

Levitus, S., Antonov, J.I., Boyer, T.P., Baranova, O.K., Garcia, H.E., Locarnini, R.A., Mishonov, A.V., Reagan, J.R., Seidov, D., Yarosh, E.S., Zweng, M.M., 2012. World ocean heat content and thermosteric sea level change (0-2000m), 1955-2010. Geophys. Res. Lett. 39. https://doi.org/10.1029/2012GL051106.

Li, Y., Han, W., 2015. Decadal sea level variations in the Indian Ocean investigated with HYCOM: roles of climate modes, ocean internal variability, and stochastic wind forcing. J. Clim. 28, 9143–9165. https://doi.org/10.1175/JCLI-D-15-0252.1.

Manasrah, R., Hasanean, H.M., Al-Rousan, S., 2009. Spatial and seasonal variations of sea level in the Red Sea, 1958-2001. Ocean Sci. J. 44, 145–159. https://doi.org/10.1007/S12601-009-0013-4/METRICS.

McDougall, Trevor J.; Barker, P.M., 2011. Getting started with TEOS-10 and the Gibbs Seawater (GSW) Oceanographic Toolbox. Scor/Iapso Wg127 28.

Mohamed, B., Abdallah, A.M., Alam El-Din, K., Nagy, H., Shaltout, M., 2019. Interannual variability and trends of sea level and sea surface temperature in the mediterranean sea over the last 25 years. Pure Appl. Geophys. 176, 3787–3810. https://doi.org/10.1007/s00024-019-02156-w.

Mohamed, B., Nagy, H., Ibrahim, O., 2021. Spatiotemporal Variability and Trends of Marine Heat Waves in the Red Sea over 38 Years. Journal of Marine Science and Engineering 2021, Vol. 9, Page 842 9, 842. Doi: 10.3390/JMSE9080842.

Mohamed, B., Skliris, N., 2022. Steric and atmospheric contributions to interannual sea level variability in the eastern mediterranean sea over 1993–2019. Oceanologia 64, 50–62. https://doi.org/10.1016/J.OCEANO.2021.09.001.

Mohamed, B., Nilsen, F., Skogseth, R., 2022. Interannual and decadal variability of sea surface temperature and sea ice concentration in the Barents sea. Remote Sens. (Basel) 14, 4413. https://doi.org/10.3390/RS14174413.

Mohamed, B., Barth, A., Alvera-Azcárate, A., 2023. Extreme marine heatwaves and cold-spells events in the Southern North Sea: classifications, patterns, and trends. Front. Mar. Sci. 10. https://doi.org/10.3389/fmars.2023.1258117.

Mulet, S., Rio, M.H., Mignot, A., Guinehut, S., Morrow, R., 2012. A new estimate of the global 3D geostrophic ocean circulation based on satellite data and in-situ measurements. Deep Sea Res. Part II 77–80, 70–81. https://doi.org/10.1016/J.DSR2.2012.04.012.

Nagy, H., Mohamed, B., Ibrahim, O., 2021. Variability of Heat and Water Fluxes in the Red Sea Using ERA5 Data (1981–2020). Journal of Marine Science and Engineering 2021, Vol. 9, Page 1276 9, 1276. Doi: 10.3390/JMSE9111276.

Palanisamy, H., Cazenave, A., Meyssignac, B., Soudarin, L., Wöppelmann, G., Becker, M., 2014. Regional sea level variability, total relative sea level rise and its impacts on islands and coastal zones of Indian Ocean over the last sixty years. Glob. Planet. Change 116, 54–67. https://doi.org/10.1016/J.GLOPLACHA.2014.02.001.

Parekh, A., Gnanaseelan, C., Deepa, J.S., Karmakar, A., Chowdary, J.S., 2017. Sea level variability and trends in the North Indian Ocean. Springer Geol. 181–192. https://doi.org/10.1007/978-981-10-2531-0_11/FIGURES/5.

Parker, A., Ollier, C.D., 2017. Is the sea level stable at Aden, Yemen? Earth Syst. Environ. 1, 1–13. https://doi.org/10.1007/S41748-017-0020-Z/FIGURES/8.

Pawlowicz, R., McDougall, T., Feistel, R., Tailleux, R., 2012. An historical perspective on the development of the Thermodynamic Equation of Seawater-2010. Ocean Sci. https://doi.org/10.5194/os-8-161-2012.

Peltier, W.R., Argus, D.F., Drummond, R., 2015. Space geodesy constrains ice age terminal deglaciation: the global ICE-6G-C (VM5a) model. J. Geophys. Res. Solid Earth 120, 450–487. https://doi.org/10.1002/2014JB011176.

Peter, B.N., Sreejith, M., Siswanto, E., 2022. Variability of Arabian Sea surface circulation and chlorophyll distribution: a remote sensing estimation. Terr. Atmos. Ocean. Sci. 33. https://doi.org/10.1007/s44195-022-00024-0.

Pettitt, A.N., 1979. A non-parametric approach to the change-point problem. Appl. Stat. 28, 126. https://doi.org/10.2307/2346729.

Raitsos, D.E., Pradhan, Y., Brewin, R.J.W., Stenchikov, G., Hoteit, I., 2013. Remote sensing the phytoplankton seasonal succession of the Red Sea. PLoS One 8, e64909. https://doi.org/10.1371/JOURNAL.PONE.0064909.

Rasul, N.M.A., Stewart, I.C.F., Nawab, Z.A., 2015. Introduction to the Red Sea: Its Origin, Structure, and Environment 1–28. Doi: 10.1007/978-3-662-45201-1_1.

Saji, N.H., Goswami, B.N., Vinayachandran, P.N., Yamagata, T., 1999. A dipole mode in the tropical Indian Ocean. Nature 401, 360–363. https://doi.org/10.1038/43854.

Saji, N.H., Xie, S.P., Yamagata, T., 2006. Tropical Indian Ocean variability in the IPCC twentieth-century climate simulations. J. Clim. 19, 4397–4417. https://doi.org/10.1175/JCLI3847.1.

Salim, M., Nayak, R.K., Swain, D., Dadhwal, V.K., 2012. Sea surface height variability in the tropical Indian Ocean: steric contribution. J. Indian Soc. Remote Sens. 40, 679–688. https://doi.org/10.1007/S12524-011-0188-X/FIGURES/8.

Schott, F.A., Xie, S.P., McCreary, J.P., 2009. Indian Ocean circulation and climate variability. Rev. Geophys. 47, 1002. https://doi.org/10.1029/2007RG000245.

Sofianos, S.S., Johns, W.E., 2001. Wind induced sea level variability in the Red Sea. Geophys. Res. Lett. 28, 3175–3178. https://doi.org/10.1029/2000GL012442/ABSTRACT.

Sofianos, S.S., Johns, W.E., 2003. An Oceanic General Circulation Model (OGCM) investigation of the Red Sea circulation: 2. three-dimensional circulation in the Red Sea. J. Geophys. Res. Oceans 108, 3066. https://doi.org/10.1029/2001JC001185.

Sofianos, S.S., Johns, W.E., 2007. Observations of the summer Red Sea circulation. J. Geophys. Res. Oceans 112. https://doi.org/10.1029/2006JC003886.

Srinivasu, U., Ravichandran, M., Han, W., Sivareddy, S., Rahman, H., Li, Y., Nayak, S., 2017. Causes for the reversal of North Indian Ocean decadal sea level trend in recent two decades. Clim. Dyn. 49, 3887–3904. https://doi.org/10.1007/S00382-017-3551-Y/FIGURES/10.

Stammer, D., Cazenave, A., Ponte, R.M., Tamisiea, M.E., 2013. Causes for contemporary regional sea level changes. Ann. Rev. Mar. Sci. 5. https://doi.org/10.1146/annurev-marine-121211-172406.

Storto, A., Masina, S., Balmaseda, M., Guinehut, S., Xue, Y., Szekely, T., Fukumori, I., Forget, G., Chang, Y.S., Good, S.A., Köhl, A., Vernieres, G., Ferry, N., Peterson, K.A., Behringer, D., Ishii, M., Masuda, S., Fujii, Y., Toyoda, T., Yin, Y., Valdivieso, M., Barnier, B., Boyer, T., Lee, T., Gourrion, J., Wang, O., Heimback, P., Rosati, A., Kovach, R., Hernandez, F., Martin, M.J., Kamachi, M., Kuragano, T., Mogensen, K., Alves, O., Haines, K., Wang, X., 2017. Steric sea level variability (1993–2010) in an ensemble of ocean reanalyses and objective analyses. Clim. Dyn. 49, 709–729. https://doi.org/10.1007/S00382-015-2554-9.

Sultan, S.A.R., Ahmad, F., El-Hassan, A., 1995. Seasonal variations of the sea level in the central part of the Red Sea. Estuar. Coast. Shelf Sci. 40, 1–8. https://doi.org/10.1016/0272-7714(95)90008-X.

Sultan, S.A.R., Ahmad, F., Nassar, D., 1996. Relative contribution of external sources of mean sea-level variations at Port Sudan, Red Sea. Estuar. Coast. Shelf Sci. 42, 19–30. https://doi.org/10.1006/ECSS.1996.0002.

Taqi, A.M., Al-Subhi, A.M., Alsaafani, M.A., 2017. Extension of satellite altimetry Jason-2 sea level anomalies towards the Red Sea coast using polynomial harmonic techniques. Mar. Geod. 40, 315–328. https://doi.org/10.1080/01490419.2017.1333549.

Taqi, A.M., Al-Subhi, A.M., Alsaafani, M.A., Abdulla, C.P., 2019. Estimation of geostrophic current in the Red Sea based on sea level anomalies derived from extended satellite altimetry data. Ocean Sci. 15, 477–488. https://doi.org/10.5194/OS-15-477-2019.

Taqi, A.M., Al-Subhi, A.M., Alsaafani, M.A., Abdulla, C.P., 2020. Improving Sea Level Anomaly Precision from Satellite Altimetry Using Parameter Correction in the Red Sea. Remote Sensing 2020, Vol. 12, Page 764 12, 764. Doi: 10.3390/RS12050764.

Thompson, P.R., Piecuch, C.G., Merrifield, M.A., McCreary, J.P., Firing, E., 2016. Forcing of recent decadal variability in the Equatorial and North Indian Ocean. J. Geophys. Res. Oceans 121, 6762–6778. https://doi.org/10.1002/2016JC012132.

Tragou, E., Garrett, C., Outerbridge, R., Gilman, C., 1999. The heat and freshwater budgets of the Red Sea. J. Phys. Oceanogr. 29, 2504–2522. https://doi.org/10.1175/1520-0485(1999)029<2504:THAFBO>2.0.CO;2.

Volkov, D.L., Lee, S.K., Gordon, A.L., Rudko, M., 2020. Unprecedented reduction and quick recovery of the South Indian Ocean heat content and sea level in 2014-2018. Sci. Adv. 6. https://doi.org/10.1126/SCIADV.ABC1151.

Wang, G., Cheng, L., Boyer, T., Li, C., 2017. Halosteric sea level changes during the Argo era. Water (Switzerland) 9, 1–13. https://doi.org/10.3390/w9070484.

Welch, P.D., 1967. The use of fast fourier transform for the estimation of power spectra: a method based on time averaging over short, modified periodograms. IEEE Trans. Audio Electroacoust. 15, 70–73. https://doi.org/10.1109/TAU.1967.1161901.

Wilks, D.S., 2011. Statistical methods in the atmospheric sciences. Academic Press.

Zhan, P., Krokos, G., Guo, D., Hoteit, I., 2019. Three-dimensional signature of the Red Sea Eddies and Eddy-induced transport. Geophys. Res. Lett. 46, 2167–2177. https://doi.org/10.1029/2018GL081387.